

Development of a 3D Velocity Model of the Canterbury, New Zealand, Region for Broadband Ground-Motion Simulation

by Robin L. Lee, Brendon A. Bradley,* Francesca C. Ghisetti, and Ethan M. Thomson

Abstract A 3D model of the geologic structure and associated seismic velocities in the Canterbury, New Zealand, region is developed utilizing data from depth-converted seismic reflection lines, petroleum and water-well logs, and cone penetration tests and is implicitly guided by existing contour maps and geologic cross sections in data-sparse subregions. The model, developed using geostatistical Kriging, explicitly represents the significant and regionally recognizable geologic surfaces that mark the boundaries between geologic units with distinct lithology and age. The model is examined in the form of both geologic surface elevation contour maps as well as vertical cross sections of shear-wave velocity, with the most prominent features being the Banks Peninsula Miocene–Pliocene volcanic edifice and the Pegasus and Rakaia late Mesozoic–Neogene sedimentary basins. The adequacy of the modeled geologic surfaces is assessed through a residual analysis of point constraints used in the Kriging and qualitative comparisons with previous geologic models of subsets of the region. Seismic velocities for the lithological units between the geologic surfaces have also been derived, thus providing the necessary information for a Canterbury velocity model for use in broadband seismic-wave propagation. The developed model also has application for the determination of depths to specified shear-wave velocities for use in empirical ground-motion modeling, which is explicitly discussed via an example.

Electronic Supplement: Figures of various horizon contour maps and tables of reflection surveys and well log details.

Introduction

The 2010–2011 Canterbury earthquake sequence (CES) produced severe ground motions which caused widespread geotechnical and structural damage throughout the Canterbury region (Kaiser *et al.*, 2012; Bradley *et al.*, 2014). The 3D geologic structure in the Canterbury subsurface was likely a salient factor in the observed structural and geotechnical damage, based on identified ground-motion basin edge and waveguide effects (Bradley and Cubrinovski, 2011; Bradley, 2012). The development of a 3D model of the Canterbury geologic structure and associated seismic velocities will provide an improved understanding of its contributions to the severe ground motions observed in the 2010–2011 CES, as well as improving predictions in future events. The principal objective for this article is the creation of a Canterbury velocity model (CantVM) for use in broadband ground-motion simulation. However, in addition, such a model can provide valuable information on the subsurface structure for

applications, such as geologic structure and restoration analyses (Ghisetti and Sibson, 2012) and depths to significant shear-wave velocity horizons (e.g., depth to 1.0 km/s shear-wave velocity $Z_{1.0}$) for use in empirical ground-motion modeling (Abrahamson and Silva, 2008). This article omits a detailed treatment of the interbedded nature of the shallow Quaternary deposits in the coastal Christchurch region of Canterbury, which is detailed in Lee *et al.* (2017).

Many geologic features in the Canterbury subsurface influence wave propagation and resulting surface ground motions, such as regional sedimentary basins and a high-velocity volcanic edifice produced by Miocene–Pliocene volcanism (Bradley, 2012; Browne *et al.*, 2012). Although the geologic structure of the Canterbury region has been investigated in the past, the quality or scope of investigations was unable to provide a regionwide framework for a consistent 3D model applied to the whole stratigraphic column (e.g., Hicks, 1989; Jongens, 2011; Ghisetti and Sibson, 2012). However, recent studies and experimental surveys coupled with previously documented results provided the

*Also at Department of Civil and Environmental Engineering, Stanford University, Stanford, California 94305.

Unit* and reflections	Equivalent formation and inferred age (Ma)
	Ground surface
Quaternary	Interbedded gravels, silts and sandstones
Pliocene	Kowai Formation (about 4–1.2 Ma)
	a. Banks Peninsula volcanics (~11–6 Ma)
Miocene	b. Tokama Siltstone (5.0 Ma) and interbedded sandstones and mudstones
Paleogene	Amuri Limestone (30 Ma) and interbedded sandstones and mudstones
Late Cretaceous	Conway and Broken River formations (65 Ma), sandstones, mudstones and coal c. Mt. Somers volcanics (89 Ma)
Basement	Torlesse Composite Terrane (>120 Ma), graywackes and schists

Figure 1. Simplified stratigraphic column detailing the general geologic sequence of the Canterbury, New Zealand, region. The considered geologic units, equivalent formations, and inferred ages in millions of years (Ma) are included. The Banks Peninsula volcanics (BPV) were emplaced during a time interval between the Miocene and Pliocene, whereas the Mt. Somers volcanics generally overlies the geologic Basement. The color scheme shown here for the geologic units is followed for the entire article. The asterisk represents the units and unit boundaries that are principally defined from a lithological perspective, hence the use of age-related unit names, used for brevity, represents the predominant age of the lithological unit, and unit boundaries are not synonymous with geologic age definitions. The color version of this figure is available only in the electronic edition.

means to produce a new 3D model of the Canterbury geologic structure that is constrained by high-quality data. Figure 1 presents a simplified stratigraphic column of the Canterbury region, summarizing the main geologic units and their relative ages in millions of years (Ma) (Forsyth *et al.*, 2008). The Canterbury stratigraphic sequence displays a complex setting caused by variations in lithology, depositional environment, and ages of the basin-infilling units (Brown and Weeber, 1992; Forsyth *et al.*, 2008). However, to produce a robust velocity model from the available data, the geologic units considered must have significantly different lithology and contrasting seismic-velocity impedance ratios, such that they are prominently evident in seismic reflection lines, used as principal constraints for building the subsurface geologic model. The sequences of geologic units explicitly modeled are herein referred to as the Quaternary, Pliocene, Banks Peninsula volcanics (BPV), Miocene, Paleogene, and Basement. The Late Cretaceous unit and Mt. Somers volcanics are assimilated into the Paleogene unit for the model, due to insufficient constraints to explicitly model them at present. As noted in the caption of Figure 1, the use of these unit names is for brevity, and because unit

boundaries are identified lithologically, they do not represent the true geologic age boundaries.

Previously, only the geologic Basement and Pliocene units (of the modeled units in this study) had been explicitly examined in 3D across the Canterbury region. Hicks (1989) and Ghisetti and Sibson (2012) both produced 3D interpretations of the geologic Basement for the wider Canterbury region, and Jongens (2011) developed a 3D interpretation for the base of the Quaternary sediments that is analogous to the top of Pliocene surface developed in this study. The scope of existing models was generally limited to onshore components and often utilized low-quality data in areas where high-quality data were not available at the time of development. Although the existing models were adequate for the purposes of their development, the CantVM presented subsequently aims to (1) expand the scope of previous models by utilizing more extensive datasets, including those offshore, and (2) remedy several limitations of the existing models by utilizing high-quality data, including recently obtained seismic reflection lines.

In this article, the details of the new 3D velocity model of the Canterbury region that explicitly characterizes five geologic units, across both onshore and offshore regions, are presented. The model spans the majority of the Canterbury basin in preparation for subsequent large-scale ground-motion simulations (e.g., South Island-wide modeling); however, a smaller subdomain (shown in subsequent figures) has been utilized with the objective of modeling ground-motion simulations of the 2010–2011 CES. An application utilizing the 3D CantVM to investigate the depth to 1.0 km/s shear-wave velocity $Z_{1,0}$ and its correlation with 30-m-averaged shear-wave velocity V_{S30} is also presented.

Summary of Adopted Datasets

Figure 2 summarizes all data sources used in the development of the CantVM and also presents the model domain. The adopted datasets for modeling the Canterbury geologic structure comprises both direct field measurements, such as several dense networks of seismic reflection lines, petroleum and water-well logs, cone penetration test (CPT) data and geologic maps of surface outcrops, as well as derived data (inferred geologic interpretations), such as existing geologic elevation contour maps and supplementary geologic cross sections in areas where a lack of field-measured data can lead to a geologically inconsistent model via the application of Kriging alone. The newly constructed geologic cross sections were specifically prepared for extending the new model into areas with scarce subsurface data, as shown in Figure 2. The seismic reflection lines provide constraint over the majority of the area relevant to the 2010–2011 CES simulation domain (although to a lesser extent onshore) and are therefore the model's principal constraint. However, water-well logs, BPV elevation contours, and CPT data (shown in Figure 3) have the most influence on the modeled BPV subsurface near its surface outcrop. Petroleum wells, water wells, and CPT records provide depths to geologic units they

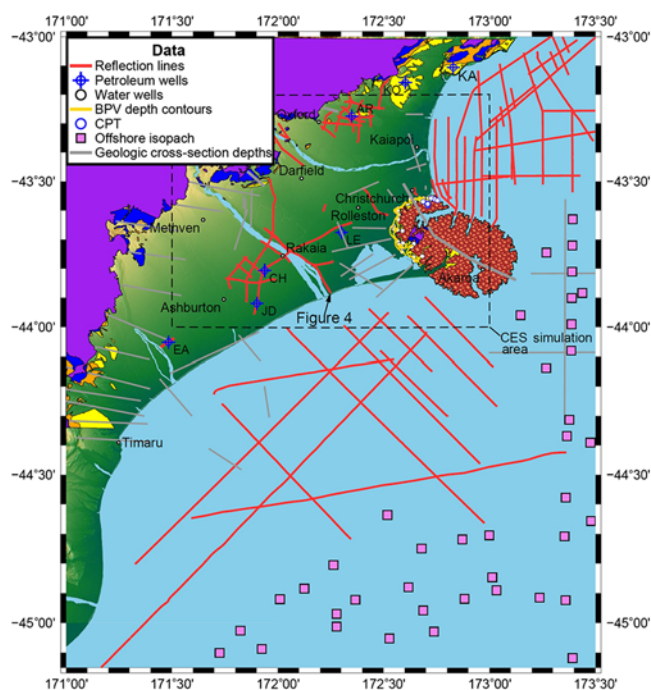


Figure 2. Summary of all data, both from direct field measurements and inferred geologic interpretation, used in the development of the Canterbury velocity model (CantVM). Areas where geologic units outcropped are shown as solid polygons. Details of the petroleum wells, for which names are abbreviated in the figure for brevity, are provided in Table S2, available in the electronic supplement to this article. The location of the seismic reflection line shown in Figure 4 is annotated. The area used for several 2010–2011 Canterbury earthquake sequence (CES) ground-motion simulations (e.g., H. Razafindrakoto *et al.*, unpublished manuscript, 2017; see [Data and Resources](#)) is also shown. Seismic velocities in the region are obtained both directly at the Kate-1 well (KA in the figure) and indirectly through the depths of geologic horizons in petroleum wells and the corresponding two-way travel time (TWTT) from seismic reflection. The color version of this figure is available only in the electronic edition.

encounter at their locations to constrain the geologic surfaces detailed in the [Geologic Surface Models](#) sections. The BPV elevation contour map, developed by [Brown and Weeber \(1994\)](#), provides elevation depths to the top of the BPV. The offshore isopach points shown in Figure 2, which were derived using isopach contours developed by [Mogg *et al.* \(2008\)](#) and bathymetry, also provide depths to the geologic unit tops in the southeast offshore area. The entire isopach maps provided by [Mogg *et al.* \(2008\)](#) were not utilized because the area is of low engineering importance. The geologic cross sections shown in Figure 2, developed based on outcrop data from geologic maps and available subsurface data, such as seismic reflection lines and the well logs previously mentioned, infer the likely position of the horizons used in the model in areas with scarce subsurface data. More details of these constraints can be found in [Lee \(2017\)](#). Collectively, the adopted datasets provide modeling constraints which span the modeled area. Because the seismic reflection lines are the principal constraints of the CantVM, details of

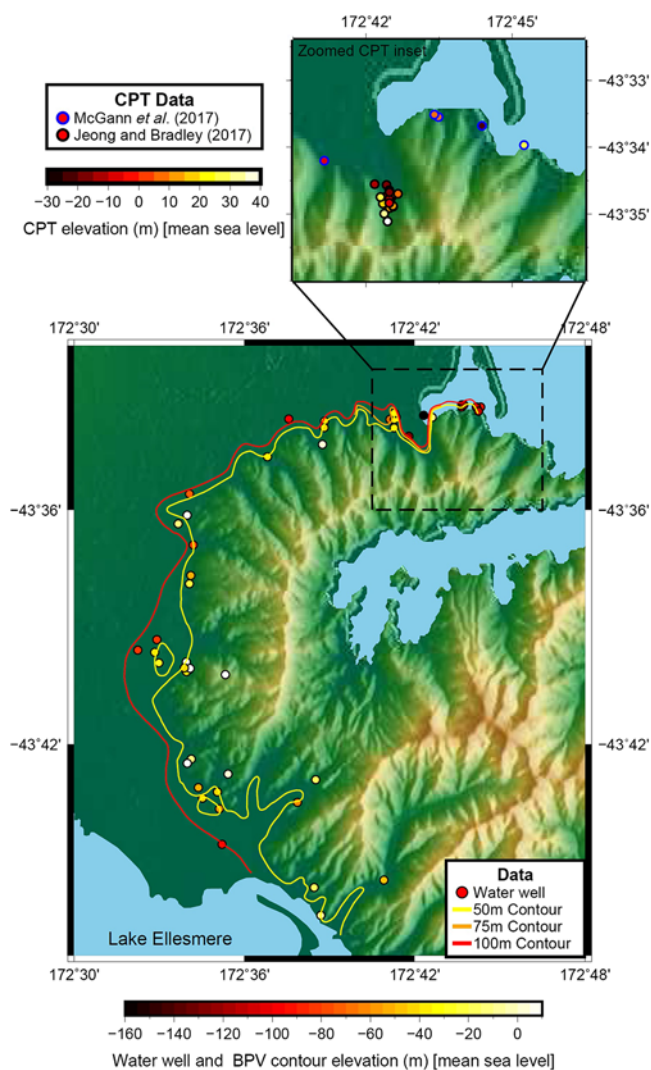


Figure 3. Spatial plots of data specifically constraining the BPV. Inset shows the cone penetration test (CPT) datasets utilized, and the main figure shows well logs identified by [Brown and Weeber \(1994\)](#) as encountering the BPV edifice and the [Brown and Weeber \(1994\)](#) elevation contour map for the BPV top surface (not including CPTs previously shown in the inset). Colors indicate elevation from the respective color scales. The color version of this figure is available only in the electronic edition.

the seismic reflection lines utilized are elaborated upon in this article.

Seismic reflection surveying is a geophysical method that utilizes the reflectivity of geologic unit boundaries as a result of impedance contrasts to produce seismic images detailing the subsurface properties and structure ([Ashcroft, 2011](#)). Seismic reflection lines are acquired in two-way travel time (TWTT) and therefore must be depth converted. Table S1 (available in the electronic supplement to this article) presents the details of the seismic reflection surveys and their associated lines utilized in this study. Additionally, Table S2 presents the list of petroleum well logs utilized in this study that were correlated against the seismic reflection lines for both their interpretation and also interval

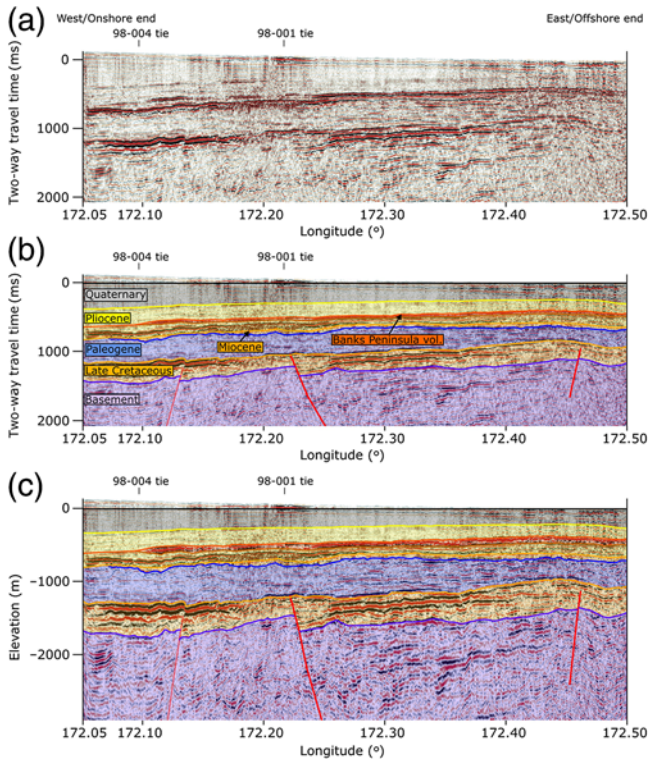


Figure 4. Illustration of interpretation and depth conversion of the 99-103 line from the Indopacific IP256-99 survey located in the Rakaia River area, including the location of two-tie line intersections with the 98-004 and 98-001 lines of the Indopacific IP256-98 survey, in which checks are carried out for consistency between the lines. The BPV is identified in the reflection line. (a) The uninterpreted reflection line in TWTT to show the common starting point for seismic reflection line processing for this study; (b) the interpreted reflection line in TWTT with marker horizons and faults; and (c) the depth-converted interpreted reflection line. All lines have 5× vertical exaggeration. The color version of this figure is available only in the electronic edition.

velocity calculations (detailed in the [Seismic Velocities of Geologic Models](#) sections).

Figure 4 illustrates the steps required to process a migrated uninterpreted seismic reflection line in TWTT into an interpreted depth-converted seismic reflection line. Figure 4a shows the uninterpreted 99-103 line of the Indopacific IP256-99 survey located in the Rakaia River area, which crosses the BPV, in TWTT, a common starting point for the seismic reflection line processing of this study. Figure 4b shows the interpreted 99-103 line where marker horizons have been traced along the identified prominent reflectors. Faults are also identified from the structural offsets observed in the reflection line. The next step is to depth-convert the reflection lines, where geologic units bounded by the marker horizons are converted to depth by multiplying the TWTT interval by representative interval velocities. The interval velocities used for the units of the model represent an average value calibrated for seismic lines that are tied to the available exploration wells and have been tested against the measured depth of the corresponding unit. These values

clearly provide a simplified description of the interval velocity that can be adequate for units with relatively uniform lithology (e.g., the Oligocene limestones, the Miocene volcanics, and the Cretaceous volcanics) but can be more approximate for some units that indeed display lateral variations in lithology (e.g., the Miocene unit). The resulting errors cannot be easily quantified without additional subsurface data and stratigraphic logs. The resulting interpreted, depth-converted reflection line is shown in Figure 4c. Figure 4 also highlights the intersection of the 99-103 line with the 98-004 and 98-001 tie lines from the Indopacific IP256-98 survey. Some existing seismic reflection lines were already available in the public domain as interpreted and depth converted, with these interpretations originally made by petroleum industry companies ([Schlumberger Geco Prakla/Indo-Pacific Energy \[NZ\] Ltd., 1998, 1999, 2000](#)). Because the stratigraphic subdivisions used by the oil industry were not necessarily the same as those required for this study, such lines have been reinterpreted for this study, as well as updated based on available new information on stratigraphic sequences in the region. The resulting depth-converted marker horizons from the seismic reflection interpretations were subsequently used as constraints for developing the geologic surfaces of the velocity model.

Geologic Surface Model Methodology

From the adopted datasets presented, it is possible to construct 3D surface models which identify boundaries between geologic units with distinct character (e.g., lithology, facies, age). The 3D surfaces developed characterize the extent and elevation of the top of each lithological unit (i.e., Pliocene, BPV, Miocene, Paleogene, and Basement units, as detailed in Fig. 1). All available geologic data were taken into account for the development of the surfaces to ensure that the model adequately represents the existing regional geology. This section discusses the salient features of the regional geology and the Kriging interpolation method employed in the model development, as well as some inherent limitations.

Considerations of Regional Geology and Model Limitations

Stratigraphic sequences are deposited during geologic time intervals that are grouped in a chronological time scale subdivided into eras, epochs, and periods (see [Forsyth *et al.*, 2008](#), for the Canterbury region). Over time, the sequence of sediments that are deposited within a sedimentary basin generally displays variations in lithology that depend on multiple factors and, for the New Zealand region, are clearly related to the tectonic setting of the depositional areas during the transition from an extensional margin to a strike-slip and transpressive margin along the present-day Pacific-Australia plate margin ([King, 2000](#)). In the South Island of New Zealand, terrestrial sediments of Late Cretaceous were followed by Paleocene–Eocene terrestrial to shallow-marine sandstones

Table 1
Geologic Unit Representations of the Canterbury Region

CantVM Unit	Period	Epoch	Wāipara	Ashley	Christchurch	South Rakaia
Quaternary	Quaternary	Holocene		Canterbury gravels		
Quaternary	Quaternary	Pleistocene		Canterbury gravels		
Pliocene	Neogene	Pliocene		Kowai Formation		
Miocene volcanics	Neogene	Miocene	Not present	Starvation Hill Basalts	Banks Peninsula volcanics group	Undiff
Miocene	Neogene	Miocene	Tokama Siltstone/Mt. Brown Formation	Undiff	Undiff	Tokama Siltstone
Miocene	Neogene	Miocene	Waikari Formation	Undiff	Undiff	Waikari Formation
Paleogene (and Late Cretaceous)	Paleogene	Oligocene		Amuri Limestone		
Paleogene (and Late Cretaceous)	Paleogene	Eocene		Homebush Sandstone		
Paleogene (and Late Cretaceous)	Paleogene	Eocene			View Hill volcanics group	Ashley Mudstone
Paleogene (and Late Cretaceous)	Paleogene	Eocene		Ashley Mudstone		Ashley Mudstone
Paleogene (and Late Cretaceous)	Paleogene	Eocene		Waipara Greensand Formation		Loburn Mudstone
Paleogene (and Late Cretaceous)	Paleogene	Paleocene	Loburn Mudstone		Not present	Loburn Mudstone
Paleogene (and Late Cretaceous)	Cretaceous	Late	Conway/Broken River Formation			Conway/Broken River Formation
Paleogene (and Late Cretaceous)	Cretaceous	Late	Conway/Broken River Formation			Mt. Somers volcanics group
Paleogene (and Late Cretaceous)	Cretaceous	Late		Torlesse Composite Terrane (Graywackes)		
Basement	Jurassic/Triassic					

and siltstones, Oligocene shallow-water limestones, Miocene marine sandstones and mudstones, and Plio-Quaternary marine to terrestrial conglomerates and gravels. The purpose of the geologic surfaces in the CantVM is to define units with contrasting velocities. Considering the Canterbury regional geology, illustrated in Table 1 (in which the CantVM column details the units explicitly modeled, the Period and Epoch columns detail the respective geologic ages each unit consists of, and the remaining columns detail the regional formations) and the most prominent reflectors in the seismic reflection lines, the surfaces identified for the CantVM separate units with contrasting lithology that were deposited through geologic time, as described above and in Figure 1. Though the proposed units provide a simplified sequence that does not incorporate the finer-scale details of lateral variations in lithology nor the time-transgressive nature of depositional surfaces throughout the study area, they nevertheless capture the relevant changes in sediment nature and supply during the tectonic evolution of the region since the Late Cretaceous, associated with marine regression and increasing input of clastic sediments from the uplifting Southern Alps through time. The uppermost geologic unit, of predominant Quaternary, is composed of alternating terrestrial gravel and marine sediments (Brown and Weeber, 1992). In this study, all Quaternary sediments are included in a single unit. However, a detailed treatment and characterization of the Quaternary formations is provided in Lee *et al.* (2017). The unit of predominantly Pliocene, bounded by the top Pliocene, BPV, and Miocene surfaces, is almost exclusively composed of the Kowai Formation, a brown weathered, graywacke-clast conglomerate with sandstone, siltstone, and mudstone with scattered shellbeds and carbonate layers. The BPV unit consists of high-velocity basaltic and trachytic lava flows in the upper regions and rhyolite and andesite lava flows in the deeper regions. The unit of predominantly Miocene is less well defined than the Pliocene unit, consisting of laterally variable, blue-gray, calcareous, sandy siltstone and brown, calcareous sandstone, locally with limestone or minor fossiliferous graywacke-clast conglomerate. The adopted unit of predominantly Paleogene embodies several formations deposited during the Oligocene, Eocene, and Paleocene. The Oligocene sediments are widely represented by the Amuri Limestone Formation across the entire region. The Eocene and Paleocene sediments generally consist of quartzose sandstones. The Late Cretaceous units have been grouped together with the Paleogene unit (as shown in Table 1), due to insufficient constraints for an explicit representation, and also primarily consists of quartzose sandstones of the Conway and Broken River formations that are widely represented in the region. The Mt. Somers volcanics, generally located in southwest Canterbury, consists of flow-banded, porphyritic rhyolite, but their subsurface position is too loosely constrained for an explicit representation, and therefore they also have been grouped together with the Paleogene unit. The geologic Basement, generally represented by the Torlesse Composite Terrane,

consists of gray, indurated, quartzofeldspathic sandstone graywackes and is reasonably consistent throughout the region (Forsyth *et al.*, 2008).

The CantVM developed in this study is principally focused on explicitly representing the sedimentary geologic horizons and Basement interface, which represent important impedance contrasts in the context of ground-motion simulation. However, the Basement structure, including the Moho, is considered in the model in a different manner. The Moho, which exists at ~ 20 km depth (Eberhart-Phillips and Bannister, 2002; Henrys *et al.*, 2004) is not modeled parametrically but is instead implicitly modeled within the Basement data of the Eberhart-Phillips *et al.* (2010) regional crustal model discussed in the [Seismic Velocities of Geologic Models](#) section.

The late Miocene–Pliocene BPV (11–6 Ma) (Forsyth *et al.*, 2008), located south of the city of Christchurch, represent a geologically significant feature (Sewell, 1988; Hampton, 2010; Ring and Hampton, 2012) that must be considered in the velocity model of the Canterbury region. These volcanic rocks have a significantly higher velocity (i.e., a modeled P -wave interval velocity of 4000 m/s, developed in the [Seismic Velocities of Geologic Models](#) section) than adjacent sedimentary geologic units (i.e., modeled P -wave interval velocities of 2100 and 2500 m/s for the Pliocene and Miocene, respectively, developed in the [Seismic Velocities of Geologic Models](#) section), which results in high impedance contrasts causing reflective wave phenomena, such as basin and waveguide effects and basin edge effects (Graves *et al.*, 1998; Joyner, 2000; Frankel *et al.*, 2009; Lee *et al.*, 2009; Bradley, 2012). The top of the BPV is well constrained, whereas the base of the BPV is to a lesser extent because many subsurface investigation techniques are unable to resolve the geologic structure through the base of volcanics or are difficult to carry out in the highland areas of the Banks Peninsula itself. For the model, the base of the BPV serves the same purpose as the top of the Miocene, and they are therefore combined because the top of the BPV is explicitly modeled separately (as shown in Table 1).

The Canterbury area is seismically active as a result of being in close proximity to the Australian and Pacific plate boundary (Sibson *et al.*, 2011; Campbell *et al.*, 2012; Ghisetti and Sibson, 2012). There are many documented faults in the Southern Alps and Canterbury foothills that are inherited from multiple episodes of tectonic deformation over time, with some of them still active in the present-day stress field. However, as the 2010–2011 CES has amply demonstrated, not all the active subsurface faults are necessarily well defined and mapped. Although all major faults are structurally important for geologic models because they eventually bound units with contrasting lithology and control the location of structural highs and depressions, they have not been specifically incorporated in this first version of the CantVM. Estimates of the horizontal and/or vertical separation of subsurface units along individual faults are in fact extremely difficult to quantify in the 3D model, especially because many

regions lack the critical subsurface data. Estimates of separation at the surface are also generally difficult in the region of the Canterbury Plains, given that many faults are buried under the sedimentary alluvial blanket. The largest faults in the area may reach maximum vertical separation of several hundreds of meters up to 1–2 km, but separation generally decreases upward and decays laterally along the fault surface (Ghisetti and Sibson, 2012; Barnes *et al.*, 2016). In all cases where seismic lines and geologic cross sections intersect the major faults, the model incorporates the change in elevation of the surfaces imposed by faulting, though the effect is generally localized along the fault surfaces and is smoothed out away from it, therefore offering some resolution of the control exerted by the faults. Further discussion of this limitation is given in the [Discussion and Conclusions](#) section.

Interpolation Method

Kriging, a generalized least-squares regression algorithm for geostatistical interpolation, was utilized to develop the geologic surfaces based on the aforementioned datasets using the Move geologic modeling software under academic license provided by Midland Valley. An exponential transition model, which determines the Kriging algorithm's spatial autocorrelation, was used for the theoretical variogram because it was found to provide the best fit to the adopted datasets among considered transition models. Variogram parameters (i.e., nugget, partial sill and range) were specifically developed for each surface, based on the field-measured data used as constraints. The theoretical exponential variogram parameters were determined by first obtaining an initial fit to the experimental variogram up to 20 km, using a least-squares approach, followed by modifications (determined via visual inspection) to the variogram parameters to provide more emphasis on shorter lag distances and to provide a moderate fit to larger lag distances (i.e., 20–40 km) if possible, the exception being the BPV, which was fitted for lag distances up to 10 km because it was Kriged over a smaller domain. Table 2 presents the adopted variogram parameters, and Figure 5 presents the variograms used for each of the geologic surfaces. Sensitivity analyses were performed throughout the determination of Kriging parameters, and minor differences between Kriging parameters in these cases were not found to significantly affect the output surfaces.

The modeled geologic surfaces were Kriged onto a rasterized grid of 1.0 km \times 1.0 km spacing, which was chosen to balance the resolution of the interpolation with the spatial density of the underlying data. The exception to this was the BPV surface, which was Kriged onto a finer grid of 200 m \times 200 m spacing, due to the higher density of well logs and CPT data near the BPV outcrop where the subsurface slopes of the volcanic edifice are steep. As the interpolation grid points do not necessarily coincide with the data used, the exact elevations of the constraints are not precisely honored, but a weighted average is assigned at the grid points instead.

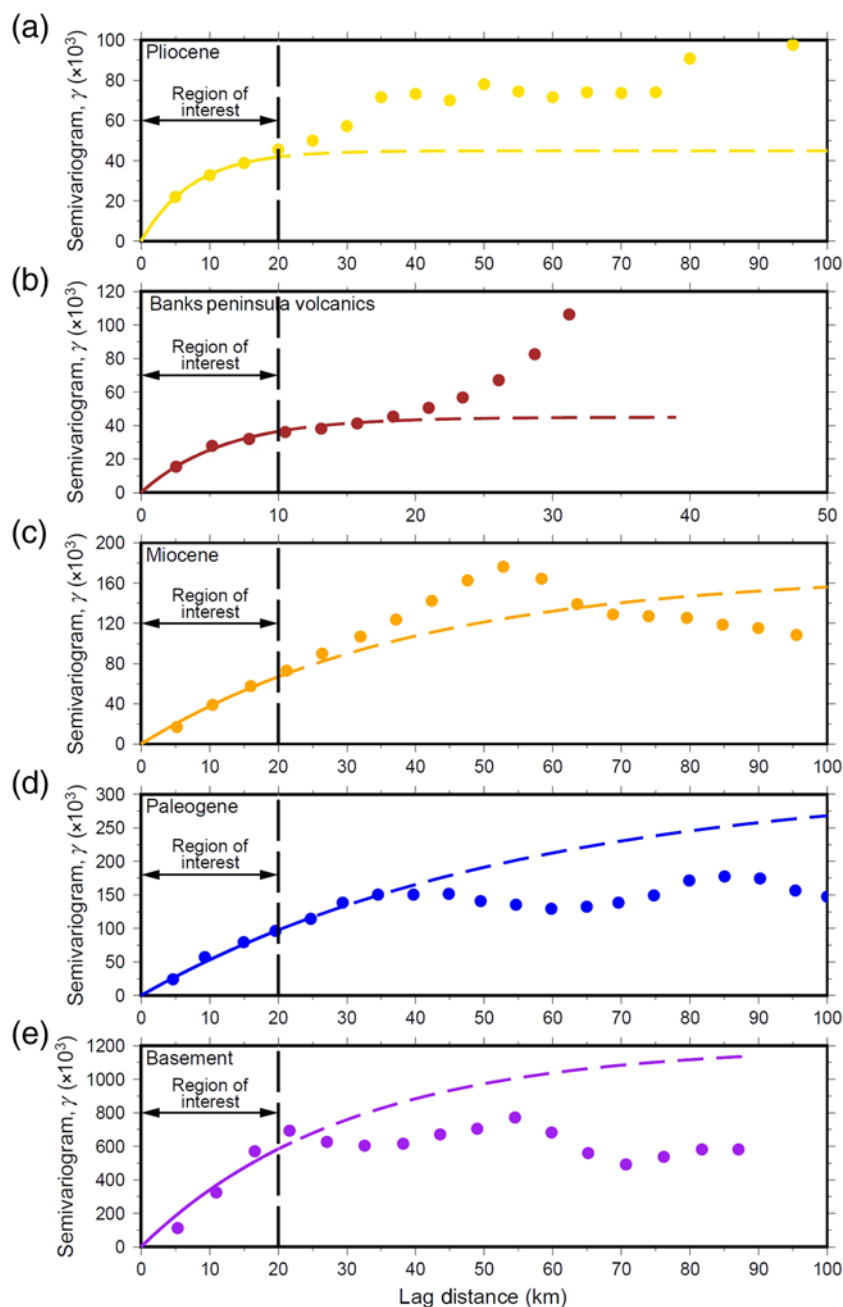


Figure 5. Experimental and theoretical exponential transition model variograms utilized in the Kriging, including the fitted regions, for the (a) Pliocene, (b) BPV, (c) Miocene, (d) Paleogene, and (e) Basement geologic surfaces. The color version of this figure is available only in the electronic edition.

Table 2

Theoretical Variogram Parameters for Each Geologic Surface

Geologic Surface	Range (km)	Partial Sill (m ²)	Nugget (m ²)
Pliocene	22.5	45,000	0
Banks Peninsula volcanics	15	40,000	0
Miocene	120	170,000	0
Paleogene	165	320,000	0
Basement	90	1,200,000	0

Geologic Surface Models

This section examines the geologic surfaces produced from the Kriging process. Figure 6 provides a 3D isometric view of the resultant surfaces in the domain utilized for several ground-motion simulations of the 2010–2011 CES which highlights their stratigraphic sequence. Detailed examinations of the top of Basement, Pliocene, and BPV surfaces are presented here by evaluating elevation contour maps of each surface. The top of the Paleogene and Miocene surfaces mirror many features observed in the Basement and Pliocene surfaces, due to common regional geologic processes, similar spatial distribution of data and interpolation assumptions and their elevation contour plots are available in the ⑤ electronic supplement. The standard deviations of each surface are also provided in the ⑤ electronic supplement. However, it is important to note that the uncertainty presented is the uncertainty of the Kriging alone, rather than the data itself because the quality of data utilized in the Kriging is not uniform and is therefore considered to be of second-order importance. It is also important to note that the top of the model is bounded by the ground-surface topography, with the sea area taken simply as 0 m elevation. The exclusion of bathymetry has minimal consequences because the sea area, at the length scales considered, is of little engineering significance.

Geologic Surface Elevation Contour Maps

Figures 7 and 8 present surface elevation contour maps (relative to mean sea level) of the marker surfaces of the top of the Basement and the top of the Pliocene, respectively. The constraints used, as shown in their respective legends, are plotted alongside the elevation contours to

provide perspective on which areas of the Kriged surfaces are well constrained. The topographic-shaded areas plotted (primarily around the Banks Peninsula and Southern Alps range-front areas) are the respective geologic unit outcrops utilized. Additionally, the surface traces of mapped faults are also plotted (Stirling *et al.*, 2012).

The top Basement surface elevation contour map (as shown in Fig. 7) shows a number of structural features. Two of the most apparent features are the two regional depressions that host Paleogene-to-Neogene sedimentary

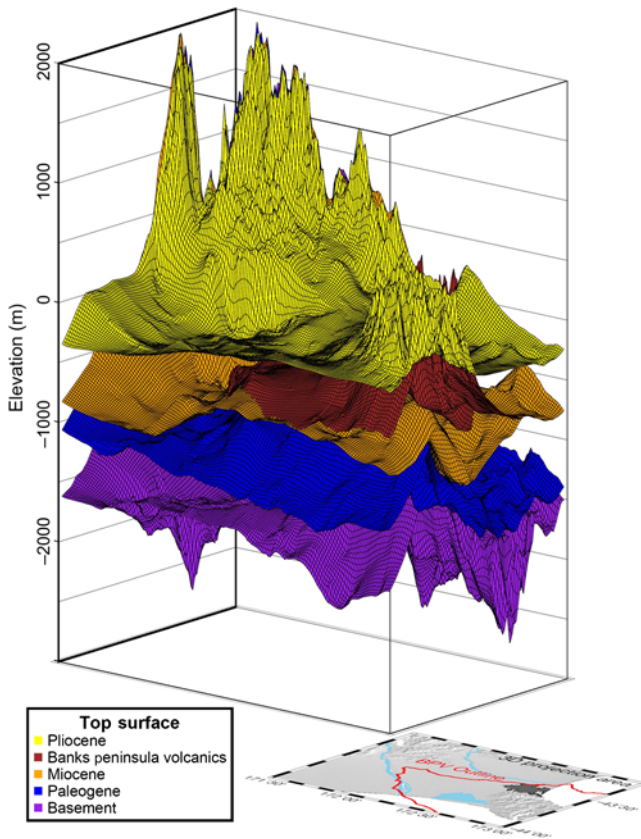


Figure 6. Isometric view of the modeled geologic surfaces overlying the domain utilized for ground-motion simulations of the 2010–2011 CES, highlighting their stratigraphic sequence. The smaller extent of BPV is displayed on the basemap, and the BPV surface can also be explicitly observed between the Pliocene and Miocene surfaces. The top of the Quaternary represents the ground surface and is therefore omitted for clarity. The color version of this figure is available only in the electronic edition.

basins, the Pegasus basin east of Kaiapoi, and the Rakaia basin in the Rakaia River area. The Pegasus basin is highly constrained by the Green Gate (Velseis Processing/Green Gate Ltd., 2006, 2007), OGS Explora (GeoSphere/Green Gate Ltd., 2005), and Kaharoa (Barnes *et al.*, 2011) seismic reflection surveys, which essentially cover the entire offshore Pegasus Bay area. The Rakaia basin is relatively constrained by the Indopacific Rakaia River lines obtained across several surveys (Schlumberger Geco Prakla/Indo-Pacific Energy [NZ] Ltd., 1998, 1999, 2000). All these geologic data show the closure of these basins against the saddle structural high, possibly controlled by easterly oriented faults (Sibson *et al.*, 2011). The location of the Banks Peninsula Miocene volcanic edifice above an inherited structural high of the basement (Ghisetti and Sibson, 2012) and the mapped outcrop of basement units in the Banks Peninsula region (Sewell, 1988; Sewell *et al.*, 1993; Hampton, 2010; Ring and Hampton, 2012) are further elements in support of the identified structural saddle. The Basement surface (as well as the other surfaces) shows the bulge associated with the double volcanic edifice structure where the Lyttelton and Akaroa

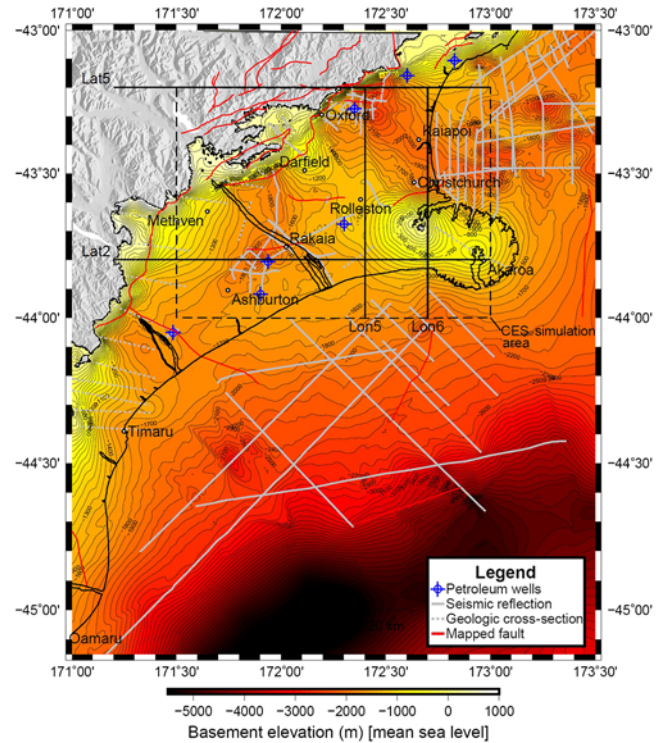


Figure 7. Top of Basement surface elevation contour map with petroleum wells, seismic reflection lines, geologic cross sections, mapped faults, and the locations of the cross sections presented in the *CantVM Geologic Cross Sections* section. The southeast corner of the plot is constrained by the offshore isopach points shown in Figure 2, that are omitted for brevity. The color version of this figure is available only in the electronic edition.

volcanoes lie (Sewell, 1988; Sewell *et al.*, 1993). The elevation of the Basement in the Lyttelton structure is inferred to reach a higher elevation than in the Akaroa structure as constrained from Basement outcropping at Gebbies pass as a result of the Gebbies Pass fault system (Forsyth *et al.*, 2008; Ring and Hampton, 2012). The saddle structure of the Basement surface between Rolleston and Darfield is less constrained by existing data but is consistent with the inferred presence of an easterly trending high delineated by strong gradients in the Bouguer gravity anomaly, as identified by gravity surveys (Hicks, 1989; Bennett *et al.*, 2000). The faults controlling this structure are poorly identified in the subsurface but possibly played a role during the 2010–2011 CES (Ghisetti and Sibson, 2012). The Basement surface also exhibits a high level of complexity in highly constrained areas, such as the Pegasus Bay area. The higher level of complexity is a reflection of the high level of detail interpreted in the constraints, particularly the reflection lines. The top Basement surface is particularly complex, due to many faults occurring in the Basement structure that do not extend to the younger units (Ghisetti and Sibson, 2012). In the context of the Basement surface, it is noted that smoothly varying elevations in regions of low data constraint likely

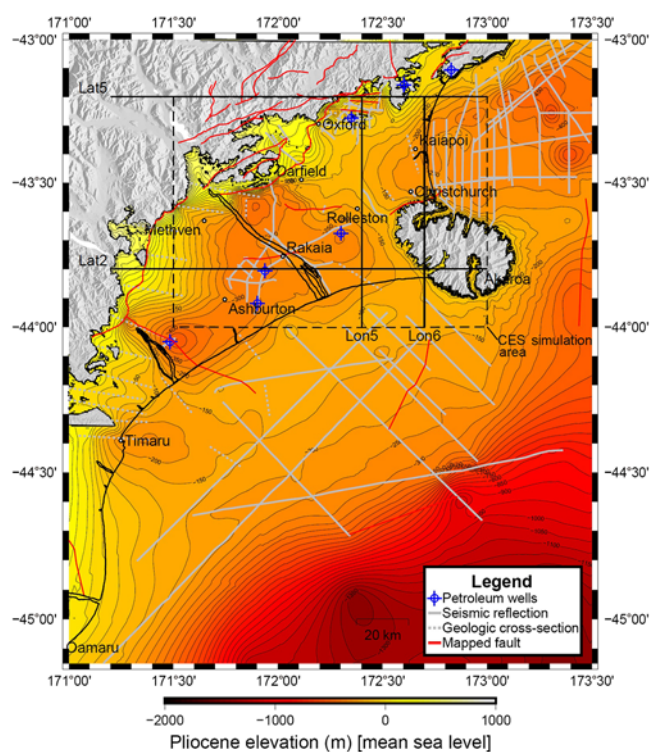


Figure 8. Top of Pliocene surface elevation contour map with petroleum wells, seismic reflection lines, geologic cross sections, mapped faults, and the locations of the cross sections presented in the [CantVM Geologic Cross Sections](#) section. The southeast corner of the plot is constrained by the offshore isopach points shown in Figure 2, that are omitted for brevity. The color version of this figure is available only in the electronic edition.

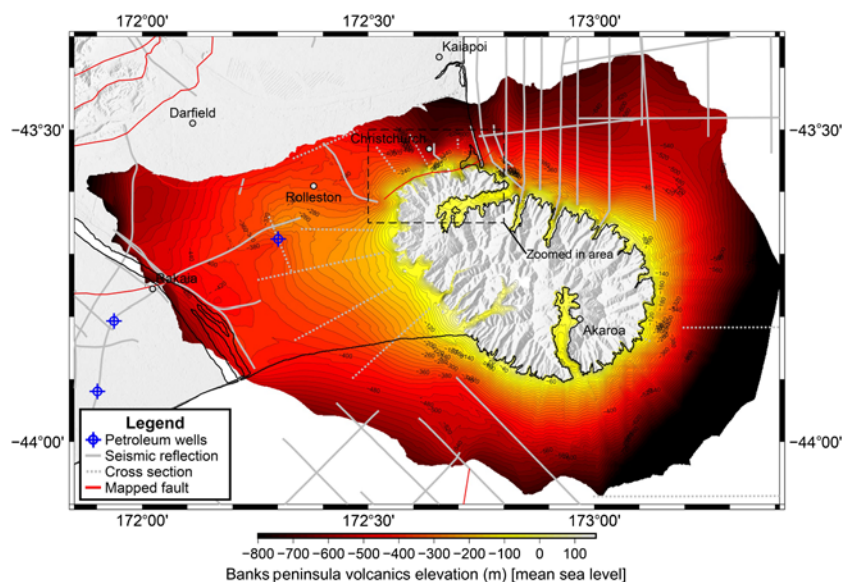


Figure 9. Top of BPV surface elevation contour map with petroleum wells, seismic reflection lines, cross sections, and mapped faults plotted. The zoomed in area plotted in [Figure S3](#) is also shown. The color version of this figure is available only in the electronic edition.

miss important Basement topography, due to unmodeled faulting.

Figure 8 illustrates the top of Pliocene surface elevation contour map, which mirrors several features of the top of the Basement surface, such as the Pegasus and Rakaia basins, the structural high at the Banks Peninsula from the Miocene–Pliocene volcanism, and the saddle structure between Rolleston and Darfield. One significant difference between the top Pliocene and top Basement surfaces is the anticline structure, the Cust Anticline, located in the Oxford area ([Barrell and Begg, 2013](#); [Mahon, 2015](#)). The top Pliocene surface has a prominent structural high in the area resulting in outcrop, whereas the top Basement surface exhibits a local geologic depression. The Cust Anticline is also mirrored by the top Miocene and top Paleogene surfaces and is highly constrained by the Indopacific Ashley River survey and Arcadia-1 well log.

Figure 9 presents the top of the BPV surface elevation contour map. The top of the BPV surface is directly observed in several well logs, inferred in several CPT data, and interpreted in seismic reflection lines. The BPV is also directly observed at its geologic outcrop. [Brown and Weeber \(1994\)](#) developed geologic elevation contours for the top of the BPV that were also utilized in the development of this model. At the location of these data, the top of the BPV is well constrained. Conversely, the eastern side of the BPV is only constrained by an inferred geologic cross section and is therefore not well constrained (but is also of low engineering importance). The two volcanoes, Lyttelton and Akaroa, form an overall conical structure as proposed by [Sewell \(1988\)](#). The general slopes on the northern, eastern, and southern sides of the Banks Peninsula are steep, whereas the western side has a more gentle dip. This is due to the subsurface

topography on which the volcanic structure overlies deeper basin structures on the offshore sides and a raised saddle structure on the western onshore side. The western extent of the BPV is also further controlled by these topographic effects because the saddle structure is on the edge of the deep Rakaia basin on the western side. [Figure S3](#) provides a close-up of the BPV top surface near the Port Hills where the well logs and contours ([Brown and Weeber, 1994](#)), CPT data ([Jeong and Bradley, 2017](#); [McGann et al., 2017](#)), and geologic outcrops ([Forsyth et al., 2008](#)) were used to constrain the steep subsurface slopes. The developed surface contours adjacent to the outcrop resemble the outline of the outcrop, following the surficial valleys and landforms. The sedimentary deposits which lie unconformably on the BPV edifice south of Christchurch result in large impedance contrasts as a result of the large stiffness

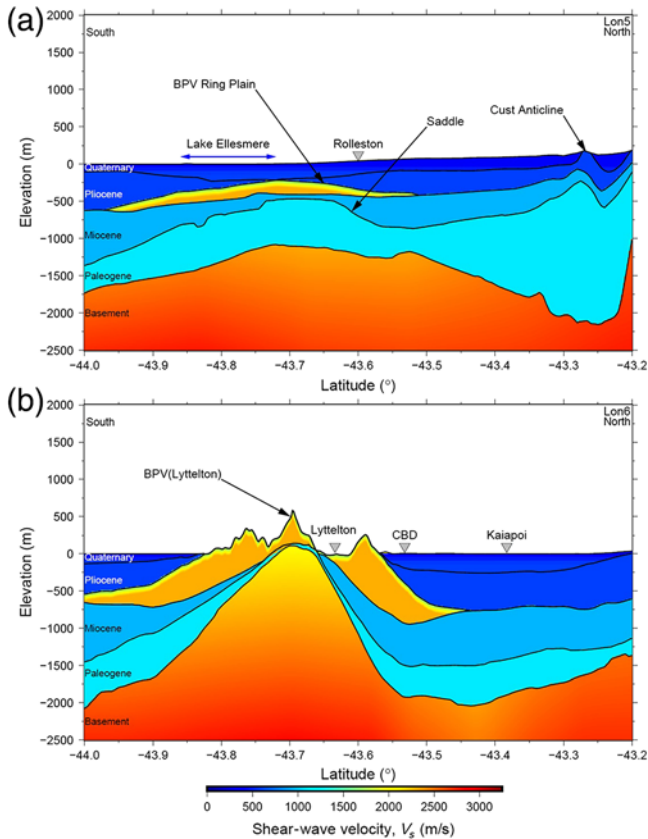


Figure 10. Cross sections of the Canterbury geologic structure and corresponding shear-wave velocities: (a) Lon5 (172.4°) and (b) Lon6 (172.7°). 20× vertical exaggeration. The color version of this figure is available only in the electronic edition.

contrast between the high-stiffness volcanic rock and adjacent low-stiffness sedimentary deposits. The base of the BPV is less well constrained than the top of the BPV because it is only observed in seismic reflection lines and inferred in gravity surveys and geologic cross sections (Forsyth *et al.*, 2008).

CantVM Geologic Cross Sections

Other than the presented elevation contour maps of the geologic unit top surfaces in Figures 7–9, additional cross sections of the geologic units and their corresponding shear-wave velocities (V_s) are presented here to provide a comprehensive evaluation of the trends and thicknesses of the various units simultaneously. Four cross sections, for which locations are shown in Figures 7 and 8, are presented in this article. Several additional cross sections are presented and discussed in Lee (2017). The velocities for the Quaternary unit are prescribed from a regional 1D velocity model, whereas the Pliocene, Miocene, BPV, and Paleogene units are prescribed velocities derived from subsurface data utilized in this study. In particular, the BPV unit includes a thin weathered layer for the top 100 m of the unit where the velocities are lower but linearly increase to the characteristic in-

terval velocity. The weathered layer was prescribed based on judgment because preliminary calculations suggested that the velocity contrasts between the BPV and the Quaternary and Pliocene were excessively large at their boundaries. The Basement unit utilizes velocities from the 3D regional crustal model from Eberhart-Phillips *et al.* (2010).

Figure 10a,b presents cross sections of constant longitude, Lon5 (172.4°) and Lon6 (172.7°), respectively. The most apparent feature encountered in the Lon5 section is the presence of the BPV ring plain (Arthur, 2013) which overlies the Miocene unit. The BPV ring plain has significantly higher velocity than adjacent geologic units and includes the aforementioned weathered layer on its top 100 m. Lon5 crosses the Ashley River area, explicitly showing the deep Basement structure, and also the Cust Anticline in the younger units identified in the Indopacific Ashley River reflection lines and Arcadia-1 well. Between latitude values of -43.8° and -43.5° , the Basement and Paleogene surfaces exhibit an elevation increase which corresponds to the structural saddle between Rolleston and Darfield. The Pliocene and Miocene surfaces do not exhibit the same elevation increase because their saddle structures are located slightly further east of the transect's location. Lon6 crosses the Lyttelton Volcano in the Banks Peninsula area where all units have a raised elevation as a result of the uplift caused by the offset of the Gebbies Pass fault system that elevates the units in the outcrop.

Figure 11a,b presents cross sections of constant latitude, Lat2 (-43.4°) and Lat5 (-44.0°), respectively. Lat2 explicitly crosses the Rakaia basin and BPV edifice, specifically the Akaroa volcano at its eastern edge, and illustrates the BPV's spatial extent in the western direction, due to favorable topography in underlying units. The Rakaia basin, deepest around 171.9° , is not only most apparent in the Basement structure but is also apparent in the overlying younger units as well. The western end of Lat5 is in the Basement outcrop, whereas the eastern end lies in the Pegasus basin. Lat5 has a Pliocene outcrop at 172.6° near the Kowai-1 well in the Ashley Forest area, which was also identified from the Christchurch area Geological Map at scale 1:250,000, where the Quaternary formations are onlapping against the top of the Pliocene unit (Forsyth *et al.*, 2008). The cross section shows steep subsurface slopes near the Basement outcrop with some abrupt changes in depth that correspond to implicit characterization of range-front faulting. Both cross sections show that the Basement structure is notably more complex and faulted, compared with the younger units.

An additional five cross sections in an oblique layout are plotted in an isometric fence diagram in Figure 12 to highlight the spatial relationship of all geologic units simultaneously across the Canterbury region. The Rakaia basin is shown along cross section 1 and the southwestern end of cross section 5 where the geologic units dip into a regional geologic depression. Cross section 2 passes through the Basement outcrop at the Southern Alps range front, along the saddle structure and through the Banks Peninsula, explic-

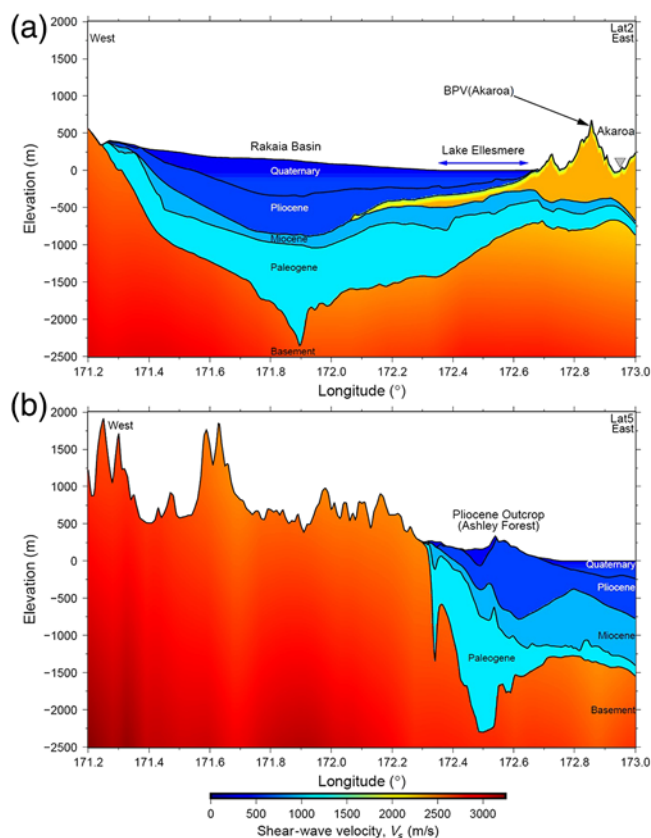


Figure 11. Cross sections of the Canterbury geologic structure and corresponding shear-wave velocities: (a) Lat2 (-43.8°) and (b) Lat5 (-43.2°). 45× vertical exaggeration. The color version of this figure is available only in the electronic edition.

itly detailing the BPV edifice. At the Lyttelton Volcano, the Basement unit outcrops at Gebbies Pass, as mapped by Forsyth *et al.* (2008). Cross section 3 passes through the Cust

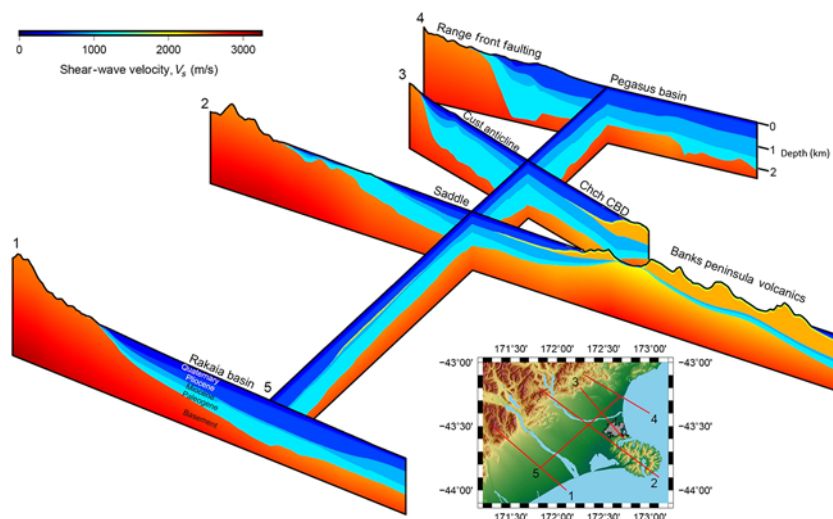


Figure 12. Fence diagram of five shear-wave velocity cross sections across the Canterbury region, highlighting the spatial relationship of the geologic units simultaneously. The color version of this figure is available only in the electronic edition.

Anticline in the northwest and the Christchurch central business district (CBD) and BPV in the southeast. Because the Christchurch CBD is located in close proximity to the BPV outcrop where the slope of the volcanic edifice is steep, the depth to the relatively stiff BPV is extremely variable and has significant implications on site response. The offshore Pegasus basin is shown along cross section 4 and the northeastern end of cross section 5. The Basement structure along cross section 4 includes several faults that were interpreted in the dense network of seismic reflection lines constraining the area. The structural saddle can be observed in cross section 5 around its intersection with cross section 2, most evidently in the Basement structure. Cross sections 1–4 also show the large variations in subsurface slopes which occur at the range front, relatively gentle in cross sections 1 and 2 and steep in cross sections 3 and 4, which are strongly dependent on the faulting present. The large variation of unit thicknesses across the Canterbury region is also apparent, although the Paleogene unit is noted to be relatively thick throughout the majority of the Canterbury region.

Assessment of Surfaces

In this section, a thorough assessment of the developed model’s geologic surfaces is carried out through a residual analysis of specific point constraints (petroleum and water-well logs, and CPT data) and qualitative comparisons with previous models. Such an analysis is necessary because the use of geostatistical Kriging does not explicitly enforce that the surface elevations honor the underlying data, instead yielding a conservative estimate of minima and maxima to provide a surface without excessive extrema (Isaaks and Srivastava, 1989). As a result, it is insightful to understand the differences between the Kriged surfaces, underlying data, and previous models.

Residual Analysis

The residual analysis of point constraints quantifies the level of agreement between the Kriged surfaces and underlying point-constraint data, and hence validates the integrity of the model surfaces. The residuals are calculated by subtracting the Kriged surface elevation from the measured elevation at each respective data point location for each relevant surface. All petroleum and water-well log and CPT residuals have been plotted here to be open about the inconsistencies that occur as a result of the numerous datasets utilized.

Water Well Logs. Figure 13 illustrates the histogram of residuals between the developed top of BPV surface and the utilized Brown and Weeber (1994) well log

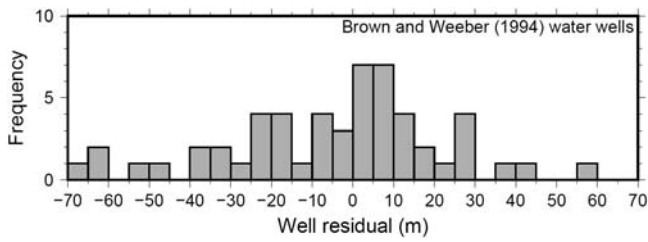


Figure 13. Histogram of the [Brown and Weeber \(1994\)](#) well log residuals, illustrating the difference between the Kriged BPV surface and the data utilized in its development.

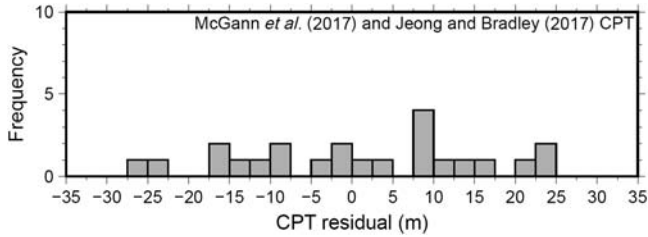


Figure 14. Histogram of the [McGann et al. \(2017\)](#) and [Jeong and Bradley \(2017\)](#) CPT-based elevation data residuals, illustrating the difference between the Kriged BPV surface and the data utilized in its development.

data. The residuals based on the well logs have a mean of -4.29 m and a standard deviation of 26.31 m. The relatively small mean suggests that there is practically no significant bias in the developed surface across the well log residuals. Maintaining small residuals in this Kriging application is difficult for several reasons, such as the steep topographic slopes making elevations very sensitive, the high density of wells in specific areas (highlighted in Fig. 3), and differences in datasets utilized where conflicts occur. The most common conflicts occur between well logs, which measure the elevation of the BPV at its location, and elevation contours, which model the macrofeatures of the top of the BPV surface, and geologic outcrop data, which lead to relatively large residuals. However, rather than discard the data that are conflicting (and therefore artificially making the resulting model appear more precise), the larger residuals are included in the analysis for transparency because they arise from inconsistencies rather than gross issues with the model. Most importantly, the overall goal of the developed model is to capture the macrofeatures of the geologic structure rather than the microfeatures that may cause localized disparities. That is, the developed regional model is not a substitute for site-specific investigations to constrain details at a specific location. With the aforementioned factors in mind, the well log residuals presented are considered to be acceptable.

Cone Penetration Test Records. Figure 14 illustrates the histogram of residuals between the top of the BPV surface and CPT-based elevation data presented in [McGann et al. \(2017\)](#) and [Jeong and Bradley \(2017\)](#). The residuals have

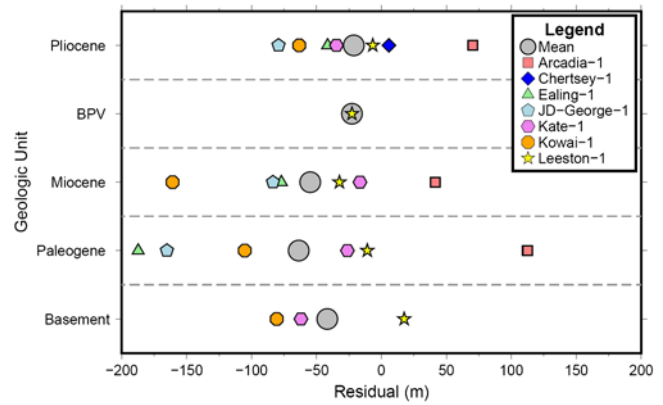


Figure 15. Petroleum well log residuals for each geologic unit considered, illustrating the difference between the Kriged surfaces and the data utilized in its development. Each well is represented by a unique symbol, allowing for well-specific trends to be identified. The color version of this figure is available only in the electronic edition.

a collective mean of 0.95 m and standard deviation of 14.64 m. Separately, the [McGann et al. \(2017\)](#) CPT data has a mean of -2.94 m and standard deviation of 5.25 m, whereas the [Jeong and Bradley \(2017\)](#) CPT data has a mean of 2.03 m and standard deviation of 16.28 m. Both collectively and separately, the means and standard deviations are small, suggesting that there is no bias and that the spread is reasonable. The [Jeong and Bradley \(2017\)](#) CPT data are very closely spaced within the Heathcote Valley area, which results in larger residuals because the chosen Kriging spacing of $200\text{ m} \times 200\text{ m}$ cannot accurately accommodate such high-density data located significantly closer together than 200 m.

Petroleum Well Logs. Figure 15 illustrates the residuals for all relevant modeled surfaces relative to the data at the petroleum well locations (see Fig. 2). The mean of the residuals for each geologic unit is shown as large circles, whereas the individual residuals are shown as the various smaller symbols, with a different shape unique to each well. It should be noted that not every geologic unit considered was encountered in each of the petroleum wells, that the BPV was only encountered once in the Leeston-1 well, and that, in general, deeper units are encountered less frequently. The mean residuals generally increase in size with unit depth, with the exception of the Basement surface; the Pliocene, Miocene, and Paleogene have mean residual values of -22 , -55 , and -64 m, respectively. The Basement has a mean of -42 m but is only encountered in three wells compared to the Pliocene, Miocene, and Paleogene, which are each encountered in six or seven wells. The standard deviations of the surfaces follow the same trend; the Pliocene, Miocene, and Paleogene have standard deviations of 50 , 69 , and 112 m, respectively. Meanwhile the Basement has a standard deviation of 52 m. The BPV surface is only encountered in one well, which has a residual of -23 m. General reasons for

the differences between the well measurements and the Kriged surface are (1) they are located on or near seismic reflection lines which have variable depth along their length and also many more points constraining the model than the single point at the petroleum well, and (2) reflection lines are depth-converted using the regional average velocity and therefore have some conflict when directly compared with the petroleum well log depths. Considering the elevation values at which the surfaces exist, the residuals are considered acceptable. The largest positive residual of the Pliocene, Miocene, and Paleogene surfaces corresponds to the Arcadia-1 well located in the Ashley River area. The Arcadia-1 well is located on the Cust Anticline structure near a local maximum with steep slopes that can cause significant variations with minor horizontal perturbations, resulting in a lower surface elevation compared with the direct well measurement.

Comparison with Previous Models

A comparison of the Kriged surfaces against previous geologic models specifically highlights improvements of the new model, as well as similarities and differences between them. Hicks (1989) and Ghisetti and Sibson (2012) both developed 3D models for the top of the Basement structure of the Canterbury region, and their interpretations are compared with the top Basement surface developed in this study. Jongens (2011) developed a 3D model for the base of the Quaternary sediments that is analogous to the top Pliocene surface developed in this study. There have been no documented or published 3D models for the BPV, Miocene, or Paleogene units to date, and therefore no qualitative comparisons can be made.

Key factors which contributed to the differences between the models were the quantity and quality of underlying data, interpolation techniques, and the resolution of the 3D regional geology at the time of development. The Kriged surfaces were found to be similar to previous geologic models in areas where the models were constrained by the same underlying data, whereas areas which were constrained by different underlying data between models were often different. For example, the new top Basement surface model and the Ghisetti and Sibson (2012) Basement model are both constrained by high-quality seismic reflection lines in the Rakaia basin and Cust Anticline areas, and therefore appear very similar in these areas. On the contrary, the Hicks (1989) model is solely based on Bouguer gravity data and therefore appears different from the new top Basement model in areas where the limitations of gravity data are prevalent (e.g., where the assumed overburden density is significantly different to the real density of the overlying sediments). The Jongens (2011) base of the Quaternary sediments model utilized several low-quality BP-Shell-Todd seismic reflection lines (Kirkaldy *et al.*, 1963) in areas which have since had high-quality reflection surveys take place. As the newly developed model is mostly constrained by high-quality data across a wider area, it is expected that the model is an improve-

ment on the characterization of the regional geology over the previous geologic models examined.

Seismic Velocities of Geologic Models

Seismic velocities (P - and S -wave velocities) and densities of the geologic units considered have been determined from well logs, reflection lines, a regional crustal model, and empirical correlations. Seismic velocities and density are important for many applications, including broadband ground-motion simulations and depths to specific shear-wave velocities for use in empirical ground-motion modeling. The various data sources provide velocities for their relevant depths but often only provide one of three required parameters, such as P - and S -wave velocities (V_P and V_S) and density (ρ). When only one parameter is provided by data, empirical correlations are utilized to provide the other required parameters. This section provides details on the various sources, methods, and empirical correlations employed to determine the velocities utilized in the CantVM.

Seismic Velocities in Well Logs

Well logs not only generally provide information on the depths in which geologic units are encountered but also sometimes provide travel-time or velocity data obtained from velocity surveys. The Kate-1 well had a checkshot survey carried out by Schlumberger Wireline Services (Styles *et al.*, 2008) that provided depths, TWTTs, and subsequently interval velocities calculated using the following equation:

$$V_{n,\text{int}} = \frac{2\Delta d}{\Delta \text{TWTT}} = \frac{2(d_{n+1} - d_n)}{\text{TWTT}_{n+1} - \text{TWTT}_n}, \quad (1)$$

in which $V_{n,\text{int}}$ is the interval velocity of the n th unit, d_n is the depth of the top of the n th unit, and TWTT_n is the TWTT of the top of the n th unit. No other well logs had direct V_P measurements.

Figure 16 presents the interval V_P data provided at the Kate-1 well (Styles *et al.*, 2008). Unique interval velocities are provided at every shot interval of ~ 50 m. Using the stratigraphy data detailed in the well log (Styles *et al.*, 2008), the interval velocity data can be segregated into the various geologic units considered, as shown in the right side of Figure 16. It is noted that Figure 16 illustrates some depth dependence for the Miocene unit. Such dependence was, however, only observable in this single unit at the Kate-1 well because other units have small thicknesses (in which the variation in interval velocity between checkshots is larger than the depth dependence, for example, for the Paleogene unit at the Kate-1 well), and such velocity information is not present at the other wells. As a result, representative average velocities for each unit were simply determined. From a macro point of view, the differences in velocities between units offer some extent of depth dependence. Although there is no depth dependence of velocities within each unit, the deeper

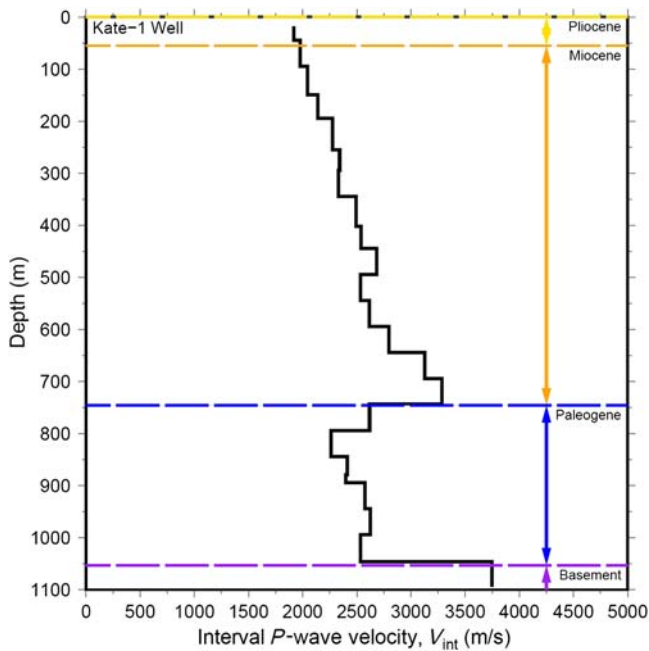


Figure 16. Interval P -wave velocities obtained from checkshot velocity surveying at the Kate-1 well (Styles *et al.*, 2008). The interval velocities are attributed to their respective geologic units, based on stratigraphic data provided for the Kate-1 well from PR3929. The color version of this figure is available only in the electronic edition.

geologic units are consolidated such that the effect of confining stress is less important than for unconsolidated sands and silts. This limitation and its implications are elaborated upon in the [Discussion and Conclusions](#) section.

Seismic Velocities from Collocated Seismic Reflection and Well Sites

Several seismic reflection lines were used in conjunction with stratigraphic data from petroleum well logs which penetrated the considered geologic horizons to determine characteristic interval velocities. Several well logs were located along (or near) seismic reflection lines, as shown in Figure 2. At the locations corresponding to the wells along the seismic reflection lines, the TWTT data for each marker horizon were extracted and then compared with the stratigraphic depths provided by well logs. The depth and TWTT intervals were then used to calculate the corresponding interval velocities. However, it is important to note that there were difficulties regarding compatibility between the resolution of geologic definitions in the well logs and seismic reflection lines (i.e., not all strata in well logs were useable for this reason because well logs followed an age-based definition, whereas seismic reflection lines identified lithological changes), which contribute to variations in the observed velocities. Figure 17 illustrates the Ealing-1 well located along the Indopacific 00-218 reflection line and the corresponding petroleum well log presented by Geological and Nuclear Sciences Ltd. (GNS). The marker horizons of the

seismic reflection lines are matched up with the stratigraphic depths from the well log providing the interval TWTT and depths required to calculate the interval velocities. This exercise is carried out at the six petroleum well logs without the checkshot surveys considered in this study, sometimes with reflection lines which were not directly used as constraints in the geologic surface development.

Overall, only one characteristic velocity was determined for each geologic unit for the wider Canterbury region by averaging the velocities calculated across all petroleum wells considered because implementation of region-based velocities was not practical, due to the small number of petroleum well logs with intersecting reflection lines relative to the variations in regional geology. Table 3 presents the derived interval V_P that are used for the depth conversion of seismic reflection lines and utilized as the seismic velocities in the CantVM, and their corresponding coefficient of variation estimated based on variability from the multiple well log data. Additionally, the corresponding V_S and ρ , calculated from correlations detailed in the [Empirical Correlations between \$P\$ - and \$S\$ -Wave Velocities and Density](#) section are also presented. V_P corresponding to the BPV and Miocene units are not as well constrained as other geologic units in the CantVM, as a result of less measured data for the BPV and the aforementioned difficulties in strata resolution for the Miocene (hence their larger coefficients of variation). To ensure that robust seismic velocities are utilized in the CantVM, additional evidence from Barnes *et al.* (2016) was considered in determining the V_P for these two geologic units, as detailed in the [Root Mean Square Stacking Velocities](#) section. It is noted that, in general across the region, the individual geologic units are relatively thin, and hence the omission of a depth dependence in the velocities for each unit is considered as a second-order error.

Root Mean Square Stacking Velocities

Interval V_P calculated by Barnes *et al.* (2016) using root mean square (rms) stacking velocities were used as additional evidence in determining the interval V_P for the less well-constrained geologic units in the CantVM, the BPV, and Miocene units (sufficiently high-resolution rms stacking-velocity data were not available for the remainder of the reflection lines). The Dix (1955) equation, shown in equation (2), was utilized to calculate the interval V_P and is derived from the geometry of down-traveling rays that are nearly vertical and incident on a series of flat and parallel layers:

$$V_{n,\text{int}} = \left[\frac{(t_{n+1} V_{\text{rms},n+1}^2 - t_n V_{\text{rms},n+1}^2)}{t_{n+1} - t_n} \right]^{\frac{1}{2}}, \quad (2)$$

in which $V_{n,\text{int}}$ is the interval velocity of the n th unit, t_n is the travel times to the n th reflector, and $V_{\text{rms},n}$ is the rms velocity of the n th unit. Barnes *et al.* (2016) computed interval V_P values of 4000 and 2510 m/s for the BPV and Miocene units, respectively, which are practically the same as the values adopted in the CantVM.

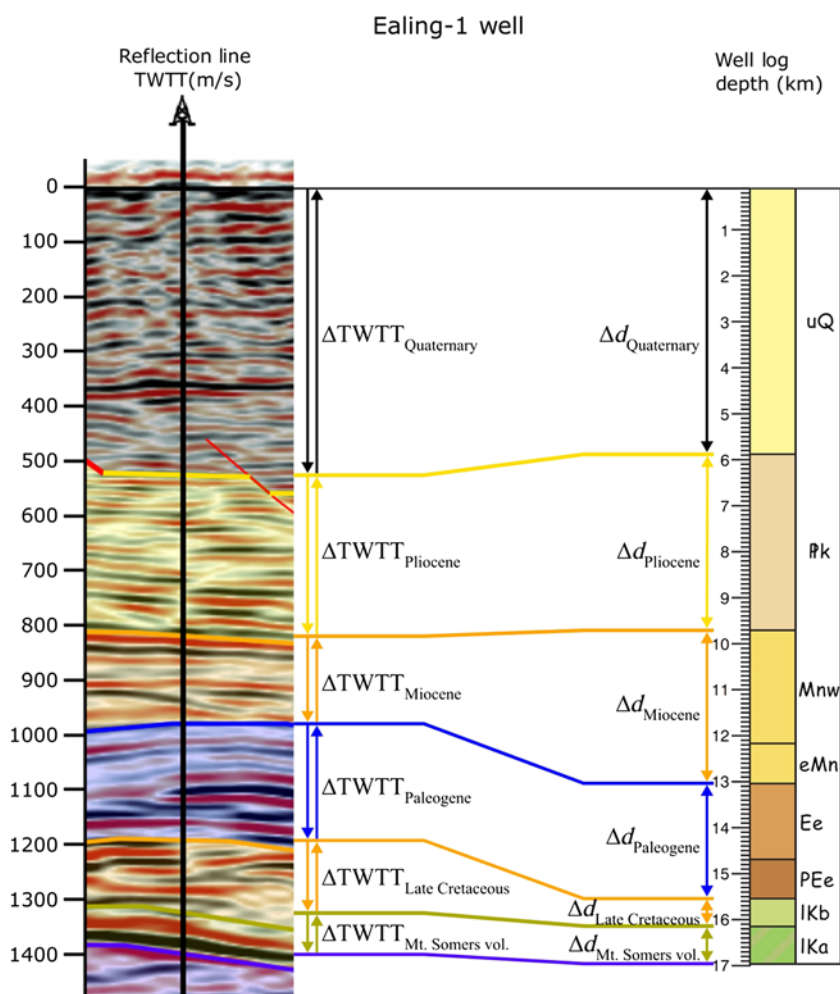


Figure 17. Interval velocity determination from seismic reflection lines and well logs illustrated at the Ealing-1 well. The TWTT at each marker horizon at the well location along the seismic reflection line is compared against the stratigraphic depths presented in documented well logs, allowing the calculation of interval P -wave velocities. The color version of this figure is available only in the electronic edition.

Empirical Correlations between P - and S -Wave Velocities and Density

To completely define the CantVM, V_p , V_s , and ρ must be defined at all points in the model. However, the field-measured datasets available often only define one of the three required parameters. In particular, seismic reflection lines only provide V_p , and currently no measured V_s data are used directly in the CantVM (although V_s profiles from surface-wave analyses will be included in the future). The exception is the New Zealand regional crustal model of [Eberhart-Phillips et al. \(2010\)](#); hereafter, EP10), used for the Basement structure of the CantVM, which provides all three required parameters. To generate all three parameters at every point, empirical correlations are employed. In particular, the [Brocher \(2005\)](#) correlations and Nafe–Drake equation ([Ludwig et al., 1970](#)) are utilized in the CantVM and are compared against the fully defined EP10 regional crustal

model to benchmark their applicability for the Canterbury region.

Figure 18 compares the V_s – V_p correlation with the EP10 regional crustal model down to a depth of 23 km below mean sea level, which roughly corresponds to the extent of applicability of the correlation. The circular symbols represent the EP10 regional crustal model data points, and the thick line represents the [Brocher \(2005\)](#) correlation. The filled area, the [Brocher \(2005\)](#) data envelope, represents the scatter of data used by [Brocher \(2005\)](#) in developing the correlation. It is important to note that the data from the EP10 model have less scatter than the [Brocher \(2005\)](#) data envelope. The correlation matches the data well at all velocities shown, with the data from the EP10 model mostly contained within the regression data envelope. At high V_p , some data fall outside the envelope, but these data correspond to points at 23-km depth, which is located in the Basement structure defined by the EP10 regional crustal model and will not utilize correlations anyway. At low V_p , the data appear to deviate slightly from the correlation but still remain within the regression data envelope. This minor deviation is acceptable, given the uncertainty inherent in both the data and correlations. Therefore, the [Brocher \(2005\)](#) V_s – V_p correlation appears valid for the Canterbury region. Comparisons between the [Brocher \(2005\)](#) V_p – V_s correlation and the Nafe–Drake equation with the EP10 regional crustal model are presented in [Lee \(2017\)](#). The

[Brocher \(2005\)](#) V_p – V_s correlation compares favorably with the regional crustal model, whereas the Nafe–Drake equation appears to systematically underpredict the regional crustal model data by roughly 2% but matches the trends observed in the data well. Despite these inconsistencies with New Zealand-specific data, we note that these empirical correlations are principally used for sedimentary soils with $V_p < 4$ km/s, which naturally will have higher uncertainty as a result of an absence of data.

Application of the Developed Canterbury Velocity Model for Depths to Constant Shear-Wave Velocity

As alluded to previously, the developed CantVM has several applications for geologic and seismic problems utilizing the model's geologic structure and associated seismic velocities. The primary application for the CantVM is 3D ground-motion simulations which utilize realistic crustal models, such as the CantVM, in seismic-wave propagation.

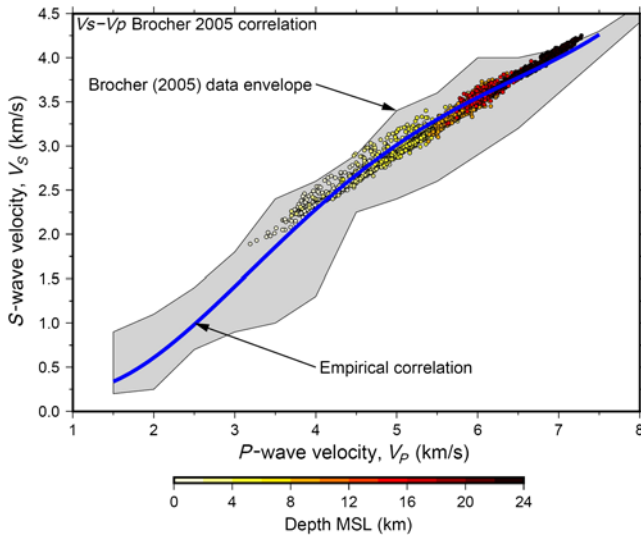


Figure 18. V_S - V_P Brocher (2005) correlation compared against gridded data from the Eberhart-Phillips *et al.* (2010) New Zealand regional travel-time tomography crustal model. Circles represent the regional crustal model data, and the thick line represents the correlation. The filled area represents the data envelope used by Brocher (2005) in developing the correlation. The color version of this figure is available only in the electronic edition.

The CantVM is currently being utilized in ground-motion simulations of the 2010–2011 CES (H. Razafindrakoto *et al.*, unpublished manuscript, 2017; see [Data and Resources](#)) and also large-scale South Island-wide simulations such as the Alpine fault rupture (Bradley *et al.*, 2017).

In addition, attention is given here to an application utilizing $Z_{1.0}$ obtained from the developed velocity model. In practical applications, $Z_{1.0}$ essentially identifies the thickness of near-surface sediments that can strongly affect observed ground motions and site response (Abrahamson and Silva, 2008). $Z_{1.0}$ is an important parameter in empirical ground-motion modeling, commonly used in ground-motion prediction equations (GMPEs) to predict intensity measures, such as peak ground acceleration and spectral acceleration (Abrahamson and Silva, 2008; Chiou and Youngs, 2008; Bradley, 2013). This section presents an investigation comparing published empirical $Z_{1.0}$ correlations with V_{S30} data from the Canterbury region, demonstrating the limitations of the correlations in a regional application, and the development of a $Z_{1.0}$ map for the Canterbury region derived from the CantVM. The provision of a $Z_{1.0}$ map would greatly benefit the use and accuracy of GMPEs in the Canterbury region.

Comparison of Regional V_{S30} and $Z_{1.0}$ Data against Empirical Correlations

$Z_{1.0}$ is a parameter that is commonly estimated using empirical correlations with V_{S30} , because measurements of $Z_{1.0}$ are significantly less common than V_{S30} (Kaklamanos *et al.*, 2011). Calculated $Z_{1.0}$ values can be used sub-

Table 3

Mean Interval Velocities and Densities of Geologic Units in the Canterbury Region with Coefficient of Variation in V_P Given in Parentheses

Geologic Unit	P -Wave Velocity (m/s)	S -Wave Velocity (m/s)*	Density (g/cc) [†]
Quaternary	1750 (5%)	457	1.78
Pliocene	2100 (6%)	677	1.95
Banks Peninsula volcanics	4000 (15%) [‡]	2282	2.39
Miocene	2500 (15%) [‡]	984	2.09
Paleogene	2850 (13%)	1281	2.19
Late Cretaceous	3000 (13%)	1413	2.22
Mt. Somers volcanics	4400 (15%)	2597	2.45
Basement [§]	5500 (10%)	3302	2.618

* S -wave velocity obtained from the Brocher (2005) correlation, using the P -wave interval velocities.

[†]Density obtained from the Nafe–Drake equation (Ludwig *et al.*, 1970; Brocher, 2005), using the P -wave interval velocities.

[‡]Additional evidence from Barnes *et al.* (2016) was used in determining these P -wave interval velocities.

[§]The Basement values listed here are just for reference and are not used in the Canterbury velocity model (CantVM) model because the Eberhart-Phillips *et al.* (2010) regional crustal velocity model is used for the Basement structure.

sequently in empirical ground-motion modeling via GMPEs. Below, an investigation comparing commonly used empirical $Z_{1.0}$ correlations to V_{S30} and $Z_{1.0}$ data from the Canterbury region is carried out. The empirical correlations considered are the Abrahamson and Silva (2008; hereafter, AS08) and Chiou and Youngs (2008, 2014; hereafter, CY08 and CY14, respectively) correlations. The regional V_{S30} data considered are values extracted from the recently developed V_{S30} model by McGann *et al.* (2017), which is primarily derived from CPT records, and V_{S30} estimates at strong-motion stations (Wotherspoon *et al.*, 2014, 2015, 2016).

Figure 19 presents the comparison of the empirical correlations and the regional V_{S30} and $Z_{1.0}$ data. The correlations are significantly different from one another at V_{S30} less than 200 m/s but begin converging to similar values at V_{S30} greater than 300 m/s. The regional V_{S30} and $Z_{1.0}$ data are subcategorized, based on whether the $Z_{1.0}$ is constrained by the depth to the top of BPV or Miocene units (because both are modeled to have, at least roughly, $V_S \geq 1.0$ km/s). The V_{S30} model data in urban Christchurch constrained by the BPV have a large range of $Z_{1.0}$ values because the V_{S30} model domain extends across the sloped BPV edifice. Despite the range in $Z_{1.0}$ that result from the BPV edifice, the V_{S30} values are relatively similar, between 150 and 250 m/s, because the top 30 m of sediments are similar across the urban Christchurch area when the BPV top surface is greater than 30 m below the ground surface (generally consisting of the Christchurch and Springston formations and occasionally the Riccarton Gravel) (Brown and Weeber, 1992). The average $Z_{1.0}$ for this subcategory is roughly 460 m, which is closest to the CY14 correlation.

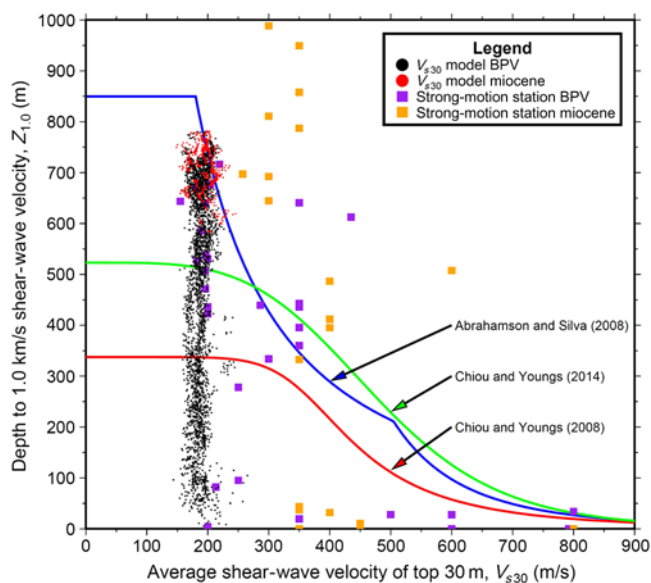


Figure 19. Comparison of regional $Z_{1,0}$ and V_{S30} data from the recently developed V_{S30} model by McGann *et al.* (2017) and strong-motion stations (Wotherspoon *et al.*, 2014, 2015, 2016) against three empirical correlations (Abrahamson and Silva, 2008; Chiou and Youngs, 2008, 2014). The data classification of BPV or Miocene indicates which geologic unit that $V_S = 1.0$ km/s is bounded by. The color version of this figure is available only in the electronic edition.

The V_{S30} model data that are constrained by the Miocene unit have $Z_{1,0}$ generally deeper than the data constrained by the BPV and also a smaller range. The average $Z_{1,0}$ value for the V_{S30} model data constrained by the Miocene unit is roughly 700 m, which fits reasonably well to the AS08 correlation. The strong-motion station data, constrained by either the BPV or Miocene, do not closely follow any of the correlations considered and appear to only have weak dependence on V_{S30} . The location of the strong-motion stations extend across the wider Canterbury region and hence encounter large variations in the geologic structure, which may be one cause of the lack of adherence to a single correlation. The observed large variations in V_{S30} and $Z_{1,0}$ data reflect the variations in regional geology and suggest that empirical correlations that provide a single $Z_{1,0}$ value dependent on V_{S30} alone are unable to accurately predict $Z_{1,0}$ consistently across the Canterbury region.

Depth to 1.0 km/s Shear-Wave Velocity Map

With the development of a regional velocity model for the Canterbury region, it is possible to directly obtain $Z_{1,0}$. Figure 20 presents the $Z_{1,0}$ map developed from the CantVM. Because of the lack of depth dependence in all layers except the Quaternary and Basement units, the $Z_{1,0}$ map is essentially constrained by the top of the BPV where it exists and the top Miocene where the BPV does not exist. $Z_{1,0}$ in areas where the Miocene (or older units) is exposed in outcrop (plotted as topography-shaded areas) are located at the ground surface. As a result, the depths shown by the map

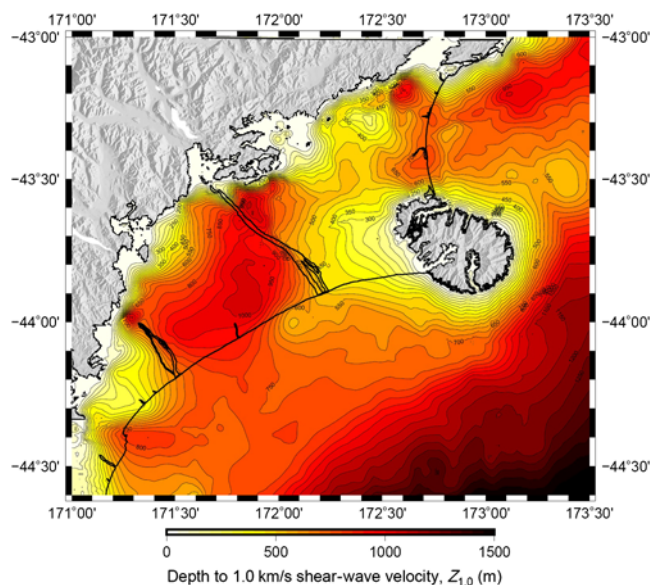


Figure 20. Modeled depth to the 1.0 km/s shear-wave velocity ($Z_{1,0}$) map of the Canterbury region. $Z_{1,0}$ is equal to the top BPV surface where it exists and the top Miocene surface otherwise, due to the assumed velocity dependence. Shear-wave velocities were calculated using the Brocher (2005) correlation. The color version of this figure is available only in the electronic edition.

reflect many structural features present in the BPV and Miocene surfaces, such as the BPV structural high, the Pegasus and Rakaia sedimentary basins, and the saddle structure. The Cust Anticline is also represented in the surface at roughly 172.4° longitude and -43.3° latitude at which $Z_{1,0}$ is shallow. Because Christchurch city is located near the BPV outcrop, the $Z_{1,0}$ values vary significantly across the Christchurch urban area (from 0 to roughly 700 m), which can cause significant variations in site response. Although the $Z_{1,0}$ map can provide values that reflect the regional geology and is an improvement over empirical correlations, it is emphasized that this is a regional representation, and site-specific investigations should still be considered where appropriate.

Discussion and Conclusions

A 3D velocity model that explicitly characterizes five geologic units with contrasting lithology deposited through time, from the Late Cretaceous to the Quaternary, was developed for the Canterbury, New Zealand, region utilizing a high-quality dataset consisting of several dense networks of seismic reflection lines, well logs, and geologic contour maps and cross sections. The residual analysis of well logs and CPT data was found to be acceptable, considering the unavoidable regional and data modeling difficulties and considering that the model was developed with the overall goal of capturing the macrofeatures of the geologic structure. The largest residuals were a result of inconsistent and spatially dense data. Seismic velocities for the modeled units were developed from well logs, seismic reflection surveys, and empirical correlations and benchmarked against the regional

crustal model developed by Eberhart-Phillips *et al.* (2010). The model has several applications, such as depths to constant shear-wave velocity horizons, as presented in this article, as well as ground-motion simulations.

The 3D CantVM developed in this study has several key limitations that have been mentioned briefly previously but are discussed here directly. These limitations are (1) the use of supplemental subsurface constraints that are based on the interpretation of the geometry of units at depth, using the projection of surface constraints in a set of geologic cross sections in areas where there is a lack of subsurface surveys; (2) the exclusion of explicit modeling of several geologic units that are instead grouped together with other CantVM units; (3) the smoothing of localized changes in elevation caused by faulting for the Kriged surfaces; (4) the simplified attribution of average seismic interval velocities in the units across the entire modeled region; and (5) the lack of depth and overburden pressure dependence of velocities within each geologic unit. The result of these limitations is a reduction in the accuracy of the model representation of the real geologic structure and geophysical properties in the relevant subregions. Examples of affected subregions include areas without field-measurement data constraints, where assimilated geologic units have significant thickness in reality, where there is an abundance of significant faulting, and where velocities vary and deviate significantly from the averaged interval velocities used. However, the specific issue of grouping the Paleogene and Late Cretaceous units together for the CantVM is expected to have negligible significance because the regional average velocity difference between the two units is only 150 m/s, and the effective media concept utilized in many wave-propagation codes (which essentially averages velocities across a spatial grid) should mitigate this issue, especially because the Late Cretaceous has relatively small thickness. The principal result of the model inaccuracies in ground-motion simulations is likely to be a reduction in the quality of seismic-wave propagation in these subregions. Such inaccuracies can be better understood by explicitly examining the errors in seismic-wave propagation via the comparison of observed and simulated ground motions. In particular, the residual errors obtained from many small-to-moderate magnitude events (an independent data source) can be used in an inversion process to improve this initial CantVM, labeled as version 1. The importance, therefore, is that the initial model developed here provides an adequately realistic representation of the modeled region, in light of available data, despite the limitations present, so that formal inversions can rapidly converge to a more accurate representation of the real geologic structure.

Data and Resources

Seismic reflection lines and wells related to petroleum exploration were obtained from the New Zealand Petroleum and Minerals (NZPAM) website, <https://data.nzpam.govt.nz/GOLD/system/mainframe.asp> (last accessed April 2015).

Water well data were provided by Environment Canterbury available at <http://canterburymaps.govt.nz/> (last accessed September 2015). The Canterbury QMap can be obtained through the GNS Science website (<http://www.gns.cri.nz/>, last accessed June 2015). The cone penetration test (CPT) data were obtained from the Canterbury Geotechnical Database (now known as the New Zealand Geotechnical Database) available at <https://www.nzgd.org.nz/> (last accessed February 2014). Topography digital elevation models were obtained from the Land Research Information Systems (LRIS) portal (<https://lris.scinfo.org.nz/>, last accessed June 2015).

Figures were prepared using Generic Mapping Tools (<http://gmt.soest.hawaii.edu/>, last accessed June 2015), and the geologic surface development was carried out using the Move geologic modeling software suite (<http://www.mve.com/>, last accessed February 2017).

The latest version of the Canterbury velocity model (CantVM) can be obtained from <https://github.com/ucgmsim/Velocity-Model> (last accessed February 2017). The other data are from the unpublished manuscript by H. Razafindrakoto, B. Bradley, and R. Graves (2017). "Broadband ground-motion simulation of the 2011 M_w 6.2 Christchurch earthquake, New Zealand."

Acknowledgments

Financial support of this research from the University of Canterbury, QuakeCoRE, the National Hazards Research Platform (NHRP), the Royal Society of New Zealand's (RSNZ) Marsden Fund, and the Rutherford Discovery Fellowship are greatly appreciated. The authors would also like to thank Matt Dodson from Environment Canterbury for providing the water well log data, Chris McGann and Seokho Jeong from the University of Canterbury for providing cone penetration test (CPT) data, John Weeber for discussion and insights on the Banks Peninsula volcanics, Matthew Hughes for his help on digital elevation models, Midland Valley for providing licenses to their Move geologic modeling software suite used to develop the model, and the two anonymous reviewers and Editor-in-Chief Thomas Pratt and Associate Editor Mark Stirling, who provided constructive critiques of this article. This is QuakeCoRE Publication Number 0192.

References

- Abrahamson, N., and W. Silva (2008). Summary of the Abrahamson & Silva NGA ground-motion relations, *Earthq. Spectra* **24**, no. 1, 67–97.
- Arthur, J. (2013). A seismic study of active faults, Canterbury, New Zealand, *M.S. Thesis*, University of Calgary, Alberta.
- Ashcroft, W. (2011). *A Petroleum Geologist's Guide to Seismic Reflection*, First Ed., Wiley-Blackwell, Chichester, United Kingdom.
- Barnes, P., C. Castellazzi, A. Gorman, and S. Wilcox (2011). *Submarine Faulting Beneath Pegasus Bay, Offshore Christchurch*, WLG2011-28, National Institute of Water and Atmospheric Research.
- Barnes, P. M., F. C. Ghisetti, and A. R. Gorman (2016). New insights into the tectonic inversion of North Canterbury and the regional structural context of the 2010–2011 Canterbury earthquake sequence, New Zealand, *Geochem. Geophys. Geosys.* **17**, no. 2, 22.
- Barrell, D. J. A., and J. G. Begg (2013). General distribution and characteristics of active faults and folds in the Waimakariri District, North Canterbury, *GNS Science Consultancy Report 2012/326*, GNS Science.
- Bennett, D., R. Brand, D. Francis, S. Langdale, C. Mills, B. Morris, and X. Tian (2000). Preliminary results of exploration in the onshore Canterbury basin, *2000 New Zealand Petroleum Conf.*, 13 pp.

- Bradley, B. A. (2012). Ground motions observed in the Darfield and Christchurch earthquakes and the importance of local site response effects, *New Zeal. J. Geol. Geophys.* **55**, no. 3, 279–286.
- Bradley, B. A. (2013). A New Zealand-specific pseudospectral acceleration ground-motion prediction equation for active shallow crustal earthquakes based on foreign models, *Bull. Seismol. Soc. Am.* **103**, no. 3, 1801–1822.
- Bradley, B. A., and M. Cubrinovski (2011). Near-source strong ground motions observed in the 22 February 2011 Christchurch earthquake, *Seismol. Res. Lett.* **82**, no. 6, 853–865.
- Bradley, B. A., S. E. Bae, V. Polak, R. L. Lee, E. M. Thomson, and K. Tarbali (2017). Ground motion simulations of great earthquakes on the Alpine Fault: Effect of hypocentre location and comparison with empirical modeling, *New Zeal. J. Geol. Geophys.* **60**, no. 3, 188–198.
- Bradley, B. A., M. C. Quigley, R. J. Van Dissen, and N. J. Litchfield (2014). Ground motion and seismic source aspects of the Canterbury earthquake sequence, *Earthq. Spectra* **30**, no. 1, 1–15.
- Brocher, T. M. (2005). Empirical relations between elastic wavespeeds and density in the Earth's crust, *Bull. Seismol. Soc. Am.* **95**, no. 6, 2081–2092.
- Brown, L. J., and J. H. Weeber (1992). *Geology of the Christchurch Urban Area, 1:25000 Geological Map*, Institute of Geological and Nuclear Sciences, Lower Hutt, New Zealand, 1 map + 104 pp.
- Brown, L. J., and J. H. Weeber (1994). Hydrogeological implications of geology at the boundary of Banks Peninsula volcanic rock aquifers and Canterbury Plains fluvial gravel aquifers, *New Zeal. J. Geol. Geophys.* **37**, no. 2, 181–193.
- Browne, G., B. Field, D. Barrell, R. Jongens, K. Bassett, and R. Wood (2012). The geological setting of the Darfield and Christchurch earthquakes, *New Zeal. J. Geol. Geophys.* **55**, no. 3, 193–197.
- Campbell, J., J. Pettinga, and R. Jongens (2012). The tectonic and structural setting of the 4 September 2010 Darfield (Canterbury) earthquake sequence, New Zealand, *New Zeal. J. Geol. Geophys.* **55**, no. 3, 155–168.
- Chiou, B. S.-J., and R. R. Youngs (2008). An NGA model for the average horizontal component of peak ground motion and response spectra, *Earthq. Spectra* **24**, no. 1, 173–215.
- Chiou, B. S.-J., and R. R. Youngs (2014). Update of the Chiou and Youngs NGA model for the average horizontal component of peak ground motion and response spectra, *Earthq. Spectra* **30**, no. 3, 1117–1153.
- Dix, C. H. (1955). Seismic velocities from surface measurements, *Geophysics* **20**, no. 1, 68–86.
- Eberhart-Phillips, D., and S. Bannister (2002). Three-dimensional crustal structure in the southern Alps region of New Zealand from inversion of local earthquake and active source data, *J. Geophys. Res.* **107**, no. B10, 2262.
- Eberhart-Phillips, D., M. Reyners, S. Bannister, M. Chadwick, and S. Ellis (2010). Establishing a versatile 3-D seismic velocity model for New Zealand, *Seismol. Res. Lett.* **81**, no. 6, 992–1000.
- Forsyth, P. J., R. Jongens, and D. J. A. Barrell (2008). *Geology of the Christchurch Area: Scale 1:250,000*, Institute of Geological and Nuclear Sciences, Lower Hutt, New Zealand, 1 map + 67 pp.
- Frankel, A., W. Stephenson, and D. Carver (2009). Sedimentary basin effects in Seattle, Washington: Ground-motion observations and 3D simulations, *Bull. Seismol. Soc. Am.* **99**, no. 3, 1579–1611.
- GeoSphere/Green Gate Ltd. (2005). *Results of Year One Exploration Work Conducted for Green Gate Ltd., PR3165*, Ministry of Economic Development.
- Ghisetti, F. C., and R. H. Sibson (2012). Compressional reactivation of E–W inherited normal faults in the area of the 2010–2011 Canterbury earthquake sequence, *New Zeal. J. Geol. Geophys.* **55**, no. 3, 177–184.
- Graves, R. W., A. Pitarka, and P. G. Somerville (1998). Ground-motion amplification in the Santa Monica area: Effects of shallow basin-edge structure, *Bull. Seismol. Soc. Am.* **88**, no. 5, 1224–1242.
- Hampton, S. (2010). Growth, structure and evolution of the Lyttelton Volcanic Complex, Banks Peninsula, New Zealand, *Ph.D. Thesis*, University of Canterbury, Christchurch, New Zealand.
- Henry, S., D. Woodward, D. Okaya, and J. Yu (2004). Mapping the Moho beneath the Southern Alps continent-continent collision, New Zealand, using wide-angle reflections, *Geophys. Res. Lett.* **31**, L17602, doi: [10.1029/2004GL020561](https://doi.org/10.1029/2004GL020561).
- Hicks, S. (1989). Structure of the Canterbury Plains, New Zealand, from gravity modeling, *Research Report No. 222*, Geophysics Division, Department of Scientific and Industrial Research.
- Isaaks, E. H., and R. M. Srivastava (1989). *An Introduction of Applied Geostatistics*, Oxford University Press, New York, New York.
- Jeong, S., and B. A. Bradley (2017). Amplification of strong ground motions at Heathcote Valley during the 2010–2011 Canterbury earthquakes: The role of 2D nonlinear site response, *Bull. Seismol. Soc. Am.* doi: [10.1785/0120160389](https://doi.org/10.1785/0120160389).
- Jongens, R. (2011). Contours for the base of Quaternary sediments under the Canterbury Plains between the Ashley and Rakaia rivers, *GNS Science Consultancy Report 2011/132*, Institute of Geological and Nuclear Sciences Limited, 17 pp.
- Joyner, W. B. (2000). Strong motion from surface waves in deep sedimentary basins, *Bull. Seismol. Soc. Am.* **90**, no. 6B, S95–S112.
- Kaiser, A., C. Holden, J. Beavan, D. Beetham, R. Benites, A. Celentano, D. Collett, J. Cousins, M. Cubrinovski, and G. Dellow (2012). The M_w 6.2 Christchurch earthquake of February 2011: Preliminary report, *New Zealand J. Geol. Geophys.* **55**, no. 1, 67–90.
- Kaklamanos, J., L. G. Baise, and D. M. Boore (2011). Estimating unknown input parameters when implementing the NGA ground-motion prediction equations in engineering practice, *Earthq. Spectra* **27**, no. 4, 1219–1235.
- King, P. R. (2000). Tectonic reconstructions of New Zealand: 40 Ma to the present, *New Zeal. J. Geol. Geophys.* **43**, no. 4, 611–638.
- Kirkaldy, P., M. Ridd, and E. Thomas (1963). Seismic survey, Canterbury Plains (interim and final reports), *Operator: BP Shell and Todd Petroleum Development Ltd., PR328*, Ministry of Economic Development.
- Lee, R. L. (2017). Development of a 3D Canterbury seismic velocity model and investigation of systematic effects through hybrid broadband ground motion simulation of small-to-moderate magnitude earthquakes, *Ph.D. Thesis*, University of Canterbury, Christchurch, New Zealand.
- Lee, R. L., B. A. Bradley, and C. R. McGann (2017). 3D models of Quaternary-aged sedimentary successions within the Canterbury, New Zealand region, *New Zeal. J. Geol. Geophys.* 1–21, doi: [10.1080/00288306.2017.1334671](https://doi.org/10.1080/00288306.2017.1334671).
- Lee, S.-J., D. Komatitsch, B.-S. Huang, and J. Tromp (2009). Effects of topography on seismic-wave propagation: An example from northern Taiwan, *Bull. Seismol. Soc. Am.* **99**, no. 1, 314–325.
- Ludwig, W. J., J. E. Nafe, and C. L. Drake (1970). Seismic refraction, *The sea* **4**, Part 1, 53–84.
- Mahon, L. E. (2015). Morphostructural and paleo-seismic analysis of fault interactions in the Oxford-Cust-Ashley fault system, Canterbury, *Master's thesis*, University of Canterbury, Christchurch, New Zealand.
- McGann, C. R., B. Bradley, and M. Cubrinovski (2017). Development of regional V_{S30} model and typical V_S profiles for Christchurch, New Zealand from CPT data and region-specific CPT– V_S correlation, *Soil Dynam. Earthq. Eng.* **95**, 48–60.
- Mogg, W., K. Aurisch, R. O'Leary, and G. Pass (2008). Offshore Canterbury basin—Beyond the shelf edge, *2008 New Zealand Petroleum Conf. Proceedings*, Sky City Convention Centre, Auckland, New Zealand, 10–15 March.
- Ring, U., and S. Hampton (2012). Faulting in Banks Peninsula: Tectonic setting and structural controls for late Miocene intraplate volcanism, New Zealand, *J. Geol. Soc.* **169**, no. 6, 773–785.
- Schlumberger Geco Prakla/Indo-Pacific Energy (NZ) Ltd. (1998). PEP 38256, onshore Canterbury, IP256-98 lines, *Operator: Indo-Pacific Energy (NZ) Limited, PR2391*, Ministry of Economic Development.
- Schlumberger Geco Prakla/Indo-Pacific Energy (NZ) Ltd. (1999). PEP 38256, Canterbury seismic survey, *Operator: Indo-Pacific Energy (NZ) Limited, PR2424*, Ministry of Economic Development.

- Schlumberger Geco Prakla/Indo-Pacific Energy (NZ) Ltd.(2000). IPE00-256 Seismic Survey. Canterbury PEP 38256, *Operator: Indo-Pacific Energy (NZ) Limited, PR2480*, Ministry of Economic Development.
- Sewell, R. (1988). Late Miocene volcanic stratigraphy of central Banks Peninsula, Canterbury, New Zealand, *New Zeal. J. Geol. Geophys.* **31**, no. 1, 41–64.
- Sewell, R., S. Weaver, and M. Reay (1993). *Geology of Banks Peninsula*, Institute of Geological and Nuclear Sciences Limited, Lower Hutt, New Zealand.
- Sibson, R., F. Ghisetti, and J. Ristau (2011). Stress control of an evolving strike-slip fault system during the 2010–2011 Canterbury, New Zealand, earthquake sequence, *Seismol. Res. Lett.* **82**, no. 6, 824–832.
- Stirling, M., G. McVerry, M. Gerstenberger, N. Litchfield, R. Van Dissen, K. Berryman, P. Barnes, L. Wallace, P. Villamor, R. Langridge, *et al.* (2012). National seismic hazard model for New Zealand: 2010 update, *Bull. Seismol. Soc. Am.* **102**, no. 4, 1514–1542.
- Styles, K., J. Coyle, and M. Beggs (2008). *Kate-1 Well Completion Report, PR3929*, Ministry of Economic Development.
- Velseis Processing/Green Gate Ltd. (2006). 2D Marine Seismic Survey PEP38260 2006 (GG-06), *PR3627*, Ministry of Economic Development.
- Velseis Processing/Green Gate Ltd. (2007). 2D Marine Seismic Survey PEP38260 2007 (GG-07), *PR3628*, Ministry of Economic Development.
- Wotherspoon, L., B. Bradley, E. Thomson, B. Cox, C. Wood, and M. Deschenes (2016). Dynamic site characterisation of Canterbury strong motion stations using active and passive surface wave testing, *EQC Report 14/663*, University of Auckland, New Zealand.
- Wotherspoon, L., R. Orense, B. Bradley, B. Cox, C. Wood, and R. Green (2014). Geotechnical characterisation of Christchurch strong motion stations, *EQC Report 12/629*, University of Auckland, New Zealand.
- Wotherspoon, L., R. Orense, B. Bradley, B. Cox, C. Wood, and R. Green (2015). Soil profile characterisation of Christchurch Central Business District strong motion stations, *Bull. New Zeal. Soc. Earthq. Eng.* **44**, no. 4, 195–204.

Department of Civil and Natural Resources Engineering
 University of Canterbury
 Private Bag 4800
 Christchurch 8140
 New Zealand
 robin.lee@pg.canterbury.ac.nz
 brendon.bradley@canterbury.ac.nz
 ethan.thomson@pg.canterbury.ac.nz
 (R.L.L., B.A.B., E.M.T.)

Terrageologica
 Ruby Bay
 Nelson 7005
 New Zealand
 francesca.ghisetti@terrageologica.com
 (F.C.G.)

Manuscript received 26 October 2016;
 Published Online 25 September 2017